

5-15-2018

Miocene-Quaternary Deformation along the Central Maynard Lake Fault, Pahrnagat Shear Zone, Nevada

Alexander Peck
antinovap@yahoo.com

Follow this and additional works at: <https://digitalscholarship.unlv.edu/thesesdissertations>



Part of the [Geology Commons](#), and the [Tectonics and Structure Commons](#)

Repository Citation

Peck, Alexander, "Miocene-Quaternary Deformation along the Central Maynard Lake Fault, Pahrnagat Shear Zone, Nevada" (2018). *UNLV Theses, Dissertations, Professional Papers, and Capstones*. 3305. <https://digitalscholarship.unlv.edu/thesesdissertations/3305>

This Thesis is protected by copyright and/or related rights. It has been brought to you by Digital Scholarship@UNLV with permission from the rights-holder(s). You are free to use this Thesis in any way that is permitted by the copyright and related rights legislation that applies to your use. For other uses you need to obtain permission from the rights-holder(s) directly, unless additional rights are indicated by a Creative Commons license in the record and/or on the work itself.

This Thesis has been accepted for inclusion in UNLV Theses, Dissertations, Professional Papers, and Capstones by an authorized administrator of Digital Scholarship@UNLV. For more information, please contact digitalscholarship@unlv.edu.

MIOCENE-QUATERNARY DEFORMATION ALONG THE CENTRAL MAYNARD LAKE
FAULT, PAHRANAGAT SHEAR ZONE, NEVADA

By

Alexander M. Peck

Bachelor of Science – Geology
University of Nevada Las Vegas
2015

A thesis submitted in partial fulfillment
of the requirements for the

Master of Science – Geoscience

Department of Geoscience
College of Sciences
The Graduate College

University of Nevada, Las Vegas
May 2018

Copyright 2018 by Alexander Peck
All Rights Reserved



Thesis Approval

The Graduate College
The University of Nevada, Las Vegas

March 29, 2018

This thesis prepared by

Alexander M. Peck

entitled

Miocene-Quaternary Deformation along the Central Maynard Lake Fault, Pahranaagat Shear Zone, Nevada

is approved in partial fulfillment of the requirements for the degree of

Master of Science – Geoscience
Department of Geoscience

Wanda J. Taylor, Ph.D.
Examination Committee Chair

Kathryn Hausbeck Korgan, Ph.D.
Graduate College Interim Dean

Rodney Metcalf, Ph.D.
Examination Committee Member

Gabrial Judkins, Ph.D.
Examination Committee Member

Barbara Luke, Ph.D.
Graduate College Faculty Representative

Abstract

MIOCENE-QUATERNARY DEFORMATION ALONG THE CENTRAL MAYNARD LAKE FAULT, PAHRANAGAT SHEAR ZONE, NEVADA

By

Alexander M. Peck

Dr. Wanda J. Taylor, Examination Committee Chair

Professor of Geoscience

University of Nevada, Las Vegas

The left-lateral Pahrnagat shear zone (PSZ) and Caliente-Enterprise zone (CEZ) exist at the boundary between two sub-provinces, the Northern (NBR) and Central Basin and Range (CBR). The PSZ contains three major ENE striking sinistral faults, including the Maynard Lake fault (MLF), which is the longest fault and marks the southern boundary of the zone. The PSZ has been suggested to be a transfer zone, but little is known about the structures along these major faults that are involved in strain transfer. These left-lateral systems exist within the Central Nevada seismic belt which has experienced significant earthquakes in recent history. Possible earthquake nucleation sites may exist along active portions of the MLF. Structures along the fault zone such as step-overs can influence the magnitude of an earthquake that could pose a risk to populated areas proximal to these faults. This Thesis focuses on the PSZ's role at the sub-province boundary, and in particular MLF to determine what structures exist along the zone, how they are involved in strain transfer and potential for earthquakes.

Map and field data suggest that the central MLF is active; it offsets Quaternary units and may pose an earthquake hazard. A resurgent fan cut by the MLF formed within the last ~10,000 years as recorded by radiocarbon sediment analysis. Map data and cross-sections reveal a transpressional zone between left-lateral, right-stepping overlapping fault strands. This transpressional step-over structure could arrest an earthquake should nucleation occur along either fault strand, which may reduce total rupture length. Moment magnitude calculations using fault length, fault segment length and an assumption of a 10 km earthquake depth suggest possible moment magnitudes between M5.7 and M6.9.

The MLF is the longest fault within the PSZ and forms the southern boundary of the PSZ. The map and kinematic data suggest that the MLF is a transfer fault that transfers strain from surrounding N-striking normal fault systems. The other major PSZ faults are also transfer faults. Thus, the PSZ is a transfer zone that accommodates differences in regional strain to the north and south of the NBR and CBR subprovince boundary. Along the boundary to the NE, hard linkage between the PSZ and CEZ cannot be confirmed, but soft linkage is possible between these distinct zones along the subprovince boundary.

Acknowledgements

This work was accomplished with the support of the UNLV Geoscience Department, my advisor, my advisory committee, family, and colleagues. Without their support this work would not have been possible, I thank them all for this opportunity.

I would like to thank the UNLV Geoscience Department for accepting me into the graduate program and providing me with consistent TA positions which provided me the funds to continue my education. I thank the office staff: Maria Ines Rojas, Elizabeth Smith, Cynthia Irwin, Maribel Simon Cruz, and Melanie Garcia, for their reliability and willingness to help with anything I needed. I would like to thank the U. S. Geological Survey for providing funding for this project through the EDMAP Award No. G16AC00101 to W.J.Taylor.

I would like to thank my peers and research group for their support, and also for those who assisted with field research: Becky Ely, Shaimaa Abd El Haleem, Mahmud Mohammed, Max Hinson, Michael Kessela, Aaron Treston, and Cameron Rickerson.

I would like to thank my family for all their support over the years. Your patience and encouraging words allowed me to follow and accomplish my dreams. For that I am forever grateful.

A special thank you goes to my advisor Wanda J. Taylor who not only provided me with this research opportunity, but has guided me towards a promising future, and will remain a close friend for years to come.

Table of Contents

Abstract	iii
Acknowledgements	v
Table of Contents	vi
List of Figures	viii
Chapter 1	1
Introduction	1
Chapter 2	3
Background	3
Regional Seismic Belts.....	6
Step-over structures.....	6
The Maynard Lake fault zone	8
Previous research along the MLF.....	8
Chapter 3	10
Methods.....	10
⁴⁰ Ar/ ³⁹ Ar dating.....	10
¹⁴ C dating.....	11
Calculation of Potential Earthquake Magnitude	12
Chapter 4	14
Stratigraphy	14
Chapter 5	17
Structural Data.....	17
Domain A	17
Delamar Lake Fault.....	18
Domain B	18
Maynard Lake Fault	19
Faults that offset Quaternary units	20
Domain C	21
Chapter 6.....	22

Structural Discussion.....	22
Maynard Lake Fault and Delamar Lake Fault as transfer faults	22
Step-over along the Maynard Lake Fault	23
Implications regarding possible future rupture along the MLF	24
Syncline.....	26
Chapter 7.....	27
Regional Interpretation.....	27
Mesozoic Deformation	27
The Maynard Lake fault and the Caliente Enterprise zone are distinct zones	27
Transfer Zone	28
Chapter 8.....	30
Conclusions.....	30
Structural Explanations.....	30
Regional.....	31
Figures.....	32
Appendix 1.....	53
Table 1. Compaction foliation measurements collected in domain A	53
Table 2. Compaction foliation measurements collected in domain B.....	54
Table 3. Compaction foliation measurements collected along the Maynard Lake fault.....	56
Table 4. Compaction foliation measurements collected from domain C.....	60
Appendix 2.....	62
Table 1. NIGL - Description and Procedures.....	62
Appendix 3.....	64
Table 1. ¹⁴ C dates from Qaf	64
Table 2. ⁴⁰ Ar/ ³⁹ Ar dating of Kane Wash Tuff Gregerson Member sample 385/386	65
Table 3. ⁴⁰ Ar/ ³⁹ Ar dating of Kane Wash Tuff Gregerson Member sample 388	67
Appendix 4.....	68
Table 1. Earthquake magnitude calculations.....	68
References.....	69
Curriculum Vitae	73

List of Figures

Figure 1 Faults and previous work.....	33
Figure 2 Basin and Range.....	34
Figure 3 Regional geologic map.....	34
Figure 4 Seismic belts.....	35
Figure 5 Step-over structures.....	36
Figure 6 Maynard Lake fault strands.....	37
Figure 7 Stereographic projection of gentle fold along the Maynard Lake fault.....	38
Figure 8 Resurgent fan.....	39
Figure 9 Sediment sample 449 hole.....	40
Figure 10 Sediment sample 450 hole.....	41
Figure 11 Sediment sample 449 bulk sediment.....	42
Figure 12 Sediment sample 450 bulk sediment.....	42
Figure 13 Sediment sample 449 carbon.....	43
Figure 14 Sediment sample 450 carbon.....	43
Figure 15 Stratigraphic column.....	44
Figure 16 Sediment sample 449 radiocarbon data.....	45
Figure 17 Sediment sample 450 radiocarbon data.....	46
Figure 18 Sample 385/386 mean age.....	47
Figure 19 Sample 388 mean age.....	48
Figure 20 Fault map.....	50
Figure 21 Rose diagrams.....	51
Figure 22 Stereographic projection domain C.....	52

Chapter 1

Introduction

Four sub-provinces within the western United States and northern Mexico make up the Basin and Range and are differentiated by basin elevation, gravity signature, heat flow, crustal thickness, and differences in deformational history. The northern Basin and Range (NBR) and central Basin and Range (CBR) meet along a zone of left-lateral movement where they are separated by two zones: the Caliente-Enterprise zone (CEZ) and Pahranaagat shear zone (PSZ). The CEZ is a left-lateral zone that extends along the NBR-CBR sub-province boundary in the east where it borders the Colorado Plateau. Counter-clockwise rotation of rocks within the zone becomes less as they approach the PSZ to the southwest (Tschanz and Pampeyan, 1970; Axen, 1998; Hudson et al., 1998). The left-lateral PSZ is characterized by three major sinistral faults including the Arrowhead Mine fault, Buckhorn fault, and the Maynard Lake fault (MLF) (Figure. 1). The northern and southern boundaries of the PSZ are defined by the Arrowhead Mine fault and the MLF, respectively. The MLF is the longest fault in the zone at ~36 km (USGS Quaternary fault and fold database, 2018). Significant movement along this fault zone occurred after ~15 Ma, as recorded by deformed Miocene volcanic rocks within the zone. Previously identified evidence of fault scarps along the MLF suggests movement has continued or the fault has been reactivated during the Quaternary (Jayko, 1990; Scott et al., 1993; U.S. Geological Survey and Nevada Bureau of Mines and Geology, 2006; Muhammad, 2016).

The PSZ and CEZ exist within the Central Nevada seismic belt (CNSB), which is a zone of active seismicity (Kreemer et al., 2010; dePolo and dePolo, 2012). This seismic belt has

produced significant earthquakes that were felt in nearby populated areas. Earthquakes include the Caliente earthquake, which produced a M 6.0 earthquake in 1966; the Saint George earthquake, which produced a M 5.3 in 1992; and the Little Skull Mountain earthquake, producing a M 5.4 in 1992 (U.S. Geological Survey and Nevada Bureau of Mines and Geology, 2006). Populated areas proximal to the PSZ vary in population size, infrastructure and distance from a possible nucleation site along the MLF within the PSZ. Two populated areas of concern include Alamo and the Las Vegas metropolitan area. Alamo has a relatively small population of ~1700 and the Las Vegas metropolitan area has a population of ~2,000,000. The city of Las Vegas resides in a valley filled with relatively soft sediments which makes the area more susceptible to ground shaking in the event of a proximal earthquake.

This research addresses the following questions: What faults exist along the central portion of the MLF, how do they interact, and how do they interact with structures that surround the zone? Which structures along the MLF are involved in strain transfer along the zone? Are there structures along the central portion of the MLF that could produce earthquakes large enough to be a hazard to nearby populated areas? What role does the PSZ play along the sub-province NBR-CBR boundary?

Chapter 2

Background

The Basin and Range can be divided into four sub-provinces; the northwestern Basin and Range (NWBR), northern Basin and Range (NBR), central Basin and Range (CBR), and the southern Basin and Range (SBR) (Figure 2). Differences in basin elevation, gravity signature, timing of the onset of extension, heat flow, and crustal thickness characterize these sub-provinces (Colgan et al., 2006; Sonder and Jones, 1999; Wernicke, 1992).

Extension began within the NBR and SBR around Oligocene to Early Miocene. During the onset of extension within the SBR, the Eastern California Shear zone (ECSZ) to the west also began activity (Sonder and Jones, 1999). Increasing extension in the NBR and SBR affected stresses in the CBR resulting in extension beginning around 18 to 14 Ma (Sonder and Jones, 1999; Bidgoli et al., 2015). Changes in the subducting Farallon plate below the CBR such as development of the slab window would have influenced basal traction and heat flow within the region (Zandt and Humphreys, 2008). Extension directions were also unique within each subprovince. The NBR primarily extended E-W, whereas the SBR extended primarily east-northeast to west-southwest (Sonder and Jones, 1999). The CBR may have temporally varied in extension direction, but was E-W to WNW-ESE throughout the sub-province (Sonder and Jones, 1999; Snow and Wernicke, 2000). The CBR extended about 1.5 times more than areas to the north (Wernicke et al., 1988; Snow and Wernicke, 2000; Kreemer et al., 2010).

On opposite sides of the NBR and CBR boundary in and near eastern Nevada, are a number of detachment faults that occurred pre-and post-Miocene volcanic activity within the region. Early onset of east-west extension during the Late Paleogene, north of the PSZ, began with the Seaman

breakaway and Stampede detachment (Taylor and Bartley, 1992; Axen et al., 1993). Later during the Miocene, to the south, the Mormon Peak detachment, Tule Springs detachment, and the Castle Cliffs detachment, and to the North, the Highland detachment began to extend east-west (Figure 3).

The PSZ and other zones of strike-slip deformation including the Kane Springs Wash fault also moved left-laterally in the Miocene (Tschanz and Pampeyan, 1970; Axen et al., 1993). Three main sinistral faults, the Arrowhead Mine fault, Buckhorn fault, and MLF, are among the most prominent faults within PSZ. The MLF is considered to be the southern boundary of the PSZ (Figure 1, A). The Kane Springs Wash fault, which lies SE of the PSZ, is a left-lateral fault that strikes NE, has 5 km or less of apparent left-lateral offset, and is thought to have been active after formation of the Kane Springs Wash caldera and during the Holocene (Best et al. 1993; Scott and Swadley, 1992, 1995; Axen, 1998) (Figure 2).

To the north of the PSZ lies one of many ENE to E-W trending lineaments (Ekren et al., 1976). Lineaments are composed of an alignment of caldera edges, topographic breaks and faults, and exhibit magnetic anomalies. These lineaments, including the Timpahute lineament (Figure 3), can be identified topographically, structurally, and through magnetic anomalies. Magnetic anomalies can be traced along topographic highs where volcanic rocks have been deposited, suggesting that deep crustal deformation was a contributing factor to caldera and volcanic activity (Ekren et al., 1976). The Timpahute lineament is geographically located ~50 km north of the MLF and trends E-W across Lincoln County (Figures 3 and 4). The lineament is made primarily of rhyolitic intrusions in the east and abuts the ends of N-trending valleys and N-striking geologic structures (Ekren et al., 1976).

The Caliente-Enterprise zone (CEZ) is a transverse zone of overall sinistral motion and counter-clockwise rotation that is ~120 km long and ranges from ~20 - 50 km wide (Figure 2).

Paleomagnetic evidence collected by Hudson et al. (1998) suggests that rocks within the CEZ, bordering the Colorado Plateau experienced small rotations, and as much as 90° of rotation about a vertical axis in the center near the Utah-Nevada border. Rocks generally become less rotated to the west and are rotated as little as ~15° just northeast of the PSZ (Axen, 1998; Hudson et al., 1998; Petronis et al., 2014) (Figure 2). Deformation may have begun as early as ~30 Ma to the north and continued through the Holocene (Axen, 1998). Extension north of the CEZ began ~30 Ma along the Stampede Detachment which is suggested to have initiated extension during the Paleogene or even the Late Mesozoic (Taylor and Bartley, 1992; Hudson et al., 1998).

South of the MLF are three N-striking faults that cut Quaternary units, Miocene volcanic rocks and Paleozoic carbonates, and are active during the Quaternary (U.S. Geological Survey and Nevada Bureau of Mines and Geology, 2006) (Figure 3). From east to west they are the Coyote Spring fault, the Sheep Range fault, and the Sheep Basin fault, which all have main N-striking fault strands that approach the MLF from the south. As these faults approach the MLF, they link into multiple older faults that abut the MLF (Jayko, 1990; Scott et al., 1990, 1993). The Coyote Spring fault consists of two segments and predominantly dips west. The northern-most segment abuts and appears to transfer strain to a left-lateral strike-slip fault that runs parallel to the MLF. Movement along the Coyote Springs fault has been confirmed as post 16 Ma and it has Quaternary fault scarps, but the actual age of the fault has not been determined (Scott et al., 1990; Scott and Swadley, 1992, 1995; U.S. Geological Survey and Nevada Bureau of Mines and Geology, 2006). The Sheep Range and Sheep Basin faults are both N-striking normal faults and the Sheep basin fault may interact directly with the MLF to the SW (Muhammad, 2016).

Regional Seismic Belts

The PSZ is located in a zone of active seismicity known as the southern Nevada seismic belt (SNSB) (Figure 4). The SNSB is postulated to be a zone of strain transfer and accommodation between the Wasatch fault zone/Intermountain seismic belt (IMSB) and the Eastern California shear zone (ECSZ) (Kreemer et al., 2010; dePolo and dePolo, 2012). Earthquake focal mechanisms show predominantly left-lateral movement within the SNSB (Kreemer et al., 2010). Particularly where the PSZ is located, strain rates may be as high as 1.8 mm/yr with a slip direction of ENE-WSW (Kreemer et al., 2010) (Figure 4). The Wasatch fault zone/Intermountain seismic belt, NE of the SNSB, is composed of steep north-south striking normal faults with a slip rate of ~0.4 mm/yr (Kreemer et al., 2010) (Figure 4). The Wasatch fault zone is a north-trending zone of active seismicity that lies along the boundary of the Basin and Range and the Colorado Plateau (Smith and Sloan, 1974). Other evidence of Quaternary/active deformation within the PSZ is supported by the identification of Holocene faults within the region (Jayko, 1990; U.S. Geological Survey and Nevada Bureau of Mines and Geology, 2006; dePolo and dePolo, 2012).

Step-over structures

Step-over structures are associated with strike-slip faults that are not continuous, but have parallel strands with overlapping fault tips. Whether a step-over is transpressional or transtensional depends on the slip sense of the strike-slip fault (sinistral or dextral) and what type of dip-slip offset is produced between fault tips. If the fault is right-stepping and sinistral, the faults produced would be reverse and create an area of transpression. If the fault is right-stepping

and is dextral, the faults produced would be normal resulting in an area of transtension (Figure 5).

The geometry of fault segmentation and the complexity of the fault segments along a fault zone play a major role in how the fault rupture will propagate and what magnitude earthquake will result (Kase et al., 2001). Where multiple faults occur along a zone and become more developed, some faults will begin to interact. These interactions result in structures such as step-overs and relay ramps (Peacock, 2002). Where an earthquake nucleates within these complex fault networks will determine how the earthquake will grow or terminate.

Step-over structures influence earthquake nucleation and propagation, and depend on fault strand interaction. Rupture may terminate at fault discontinuities or jump through them. Earthquake nucleation which occurs on or near a particular fault tip may propagate across a step-over and onto the adjacent overlapping fault strand (Oglsby, 2008). Dynamic models produced by Oglsby (2005, 2008) and Kase et al. (2001) both suggest that overlapping fault strands that have an area of transtension between them allow for easy earthquake propagation from one strand to the other by using the normal faults that connect the strands to jump across. Rupture propagation across an extensional (transtensional) step-over is considered to be more likely than through a compressional step-over under similar circumstances; however, earthquake propagation can occur with a compressional step-over if the point of earthquake nucleation is on the linking faults rather than a fault strand (Oglesby, 2005). In other words, if an earthquake nucleates on the linking faults within a transpressional step-over, slip is likely to continue away from the point of nucleation, along adjacent fault strands. In contrast, earthquakes that propagate toward transpressional step-overs are likely to be arrested at the step-over (Figure 5).

Distance between overlapping fault segments and initial displacement along a fault segment are important factors when determining whether an earthquake can propagate from one segment to the other. Earthquake propagation may arrest when fault segments are 4-5 km apart and initial fault displacement along a segment is <5 m (Lettis et al., 2002). If the fault segments are 1-2 km apart, initial fault displacement of ≤ 3 m can propagate across the step-over (Lettis et al., 2002). Kase and Kuge (2001), who ran 3D numerical simulations of fault step-over propagations, concluded that not only do fault geometries and location of the fault limbs influence rupture across step-overs, but depth of the upper edge of the faults from the Earth's surface is also important. Faults that are closer to the Earth's surface have a greater ability to propagate an earthquake or slip to a second strand, resulting in a larger rupture than faults at depth which may arrest as they approach the fault edge.

The Maynard Lake fault zone

The MLF comprises multiple interacting sinistral and oblique fault strands which cut Miocene volcanic rocks and Quaternary sediments. Faults mapped within the fault zone are primarily NE-SW striking with similar steep dips and create a fault network, with multiple fault strands, step-overs, restraining bends, and folds (Figures 6 and 7). About 5.5 km of the MLF was mapped within the study area along the central portion of the fault zone.

Previous research along the MLF

Previously mapped geological features to the NE and SW of the study area support extensive Quaternary faulting along the MLF zone. Geological maps produced by Scott et al. (1990, 1993), including the Delamar Lake quadrangle and a preliminary geologic map of the Delamar 3 NW quadrangle, show the accurate location of the MLF which can be followed to the NE for about 15

km. The Delamar Lake quadrangle map to the NE indicates Quaternary faulting cutting alluvium and is the most distant evidence to the NE that supports Quaternary movement along the fault zone (Figure 1, B).

Muhammad (2015) produced a geological map SW of the study area where strands of the MLF were identified. At least two faults mapped within this area cut Quaternary units providing evidence for the continuation of Quaternary fault activity along the MLF zone to the SW.

Continuing SW, mapping was also completed by Miera (2015) who identified a continuation of the MLF. Combined geological mapping results in a total of ~35 km of identified Quaternary faulting along the MLF zone.

Chapter 3

Methods

Several methods and tools were utilized to produce and interpret data collected from the study area along the central portion of the MLF. To gather more precise data, mapping at 1:12000 allowed for more detailed placement of units and structures within the study area (Plate 1). A Brunton compass was used to determine tuff compaction foliation and bedding orientations. A Garmin Fortrex GPS was used to maintain an accurate log of measurement data collected and its geographical location (Appendix 1). When identifying units in the field, Best et al.'s (1993) model and total phenocryst percentages, and regional tuff identification table was consulted. While there is much variation across and within certain units within the study area, Best et al.'s (1993) phenocryst assemblage values allowed for quick identification of the more commonly occurring tuffs in the area. On completion of field data collection, stereographs were created to classify folds (Allmendinger, 2013). Rose diagrams were created to delineate fault sets and networks. Cross-sections (A-A' – D-D') were produced with a fence diagram to aid in surface and subsurface analysis (Plate 2).

⁴⁰Ar/³⁹Ar dating

⁴⁰Ar/³⁹Ar dating of sanidines from separate cooling units of Kane Wash Tuff (Tkg2 and Tkg1) that are present within the study area was conducted using NIGL (Nevada Isotope Geochronology Laboratory), located at the University of Nevada Las Vegas. Isotope analysis of two samples, 388 (Tkg1) and 385/386 (Tkg2), was necessary to distinguish the separate cooling units and to determine the youngest age of the Kane Wash Tuff.

Before NIGL could begin analysis, rock samples free of weathering were collected and brought back to the rock lab where the process of crushing, sieving, picking, and washing resulted in sanidine crystals that were free of contaminants. Approximately 60 sanidines were collected from each of the two samples at sizes between 0.30 mm and 0.60 mm (399 and 385/386) and sent to NIGL for selection of sanidines suitable for accurate $^{40}\text{Ar}/^{39}\text{Ar}$ dating. Once the two samples were prepared in the NIGL lab, they were sent off to Denver, Colorado to be placed in a 1 MW TRIGA type reactor for 7 hours. After the irradiation process was complete, the samples were returned to NIGL for final analysis including fusing the sanidine crystals with a 20 W CO_2 laser. Gasses produced from fusion of crystals were admitted to a MAP 215_50 mass spectrometer where upon further analysis, reliable age data for the two cooling units were produced. For more detail on the procedure that NIGL followed for this analysis, please review Appendix 2, table 1.

^{14}C dating

Within the study area an alluvial fan (Qaf) is cut by the MLF, and overlapped by a bouldery resurgent fan with ~1 m of normal and a small amount of left offset of Quaternary conglomerate (Qtc) (Plate 1). In order to bracket the timing of last measurable movement along the MLF, two sediment samples from different locations (Figure 8) and depths were collected from the alluvial fan (Qaf) and sent to Beta Analytic in Miami, Florida for radiocarbon analysis. Soil sample 449 was collected at 30 cm (1 foot) below the surface of the fan. The depth was chosen to reduce contamination from surface carbonates (Figure 9). Sample 450 was collected at 60 cm (2 feet) below the fan surface (Figure 10). In order to limit contamination, tools used for digging were decontaminated before use, and samples collected were transferred directly to aluminum foil and

sealed before leaving the collection site. Each sample (including foil) weighed 900 gm (2 pounds) (Figures 11 and 12).

Once received by Beta Analytic, the samples were washed to extract datable carbon resulting in 27,149 mg of carbon from sample 449 and 20,006 mg from sample 450 (Figures 13 and 14). To measure the ^{14}C content of the material separated from the sample, National Electrostatics Corp (NEC) mass spectrometers and thermo isotope ratio mass spectrometers (IRMS) were employed. To obtain an accurate conventional radiocarbon age (CRA), standards such as the Libby half-life; a secondary standard as the modern radiocarbon standard, Vienna Pee Dee Belemnite (VPDB) international reference standard for carbon isotopes; and the assumption that radiocarbon levels are constant were utilized (Beta Analytics, 2018).

Calculation of Potential Earthquake Magnitude

Earthquake size can be determined from a number of geometrical parameters that result from earthquake rupture. Extensive data was compiled by Wells and Coppersmith (1994) who categorized known earthquakes by the magnitude, moment magnitude, slip type, and surface rupture length. Strong correlations between these factors allowed for the development of empirical equations (Wells and Coppersmith, 1994), which can be implemented to calculate moment magnitude (M) from surface rupture length: $M = 5.08 + 1.16 \log (\text{SRL})$ (where SRL is surface rupture length in km), or maximum displacement $M = 6.69 + 0.74 \log (\text{MD})$ (where MD is maximum displacement in km) both with a 95% accuracy. Hanks and Bakun (2002) present an adjusted model for larger magnitude earthquakes including the equation $M = \log A + 3.98 \pm 0.03$, where A (fault area) is $\leq 537 \text{ km}^2$ and $M = 4/3 \log A + 3.07 \pm 0.04$, where $A > 537 \text{ km}^2$. Anderson et al. (1996, 2017) developed and presented the equation, $M_w = 5.12 + 1.16 \log L - 0.20 \log S$, that incorporates L (length in km), and S (slip rate mm/yr). This equation can be

applied to faults where the slip rate is known. I utilized all three equations in this study for a better analysis of earthquake magnitude along the MLF.

Chapter 4

Stratigraphy

Stratigraphy along the central portion of the MLF within the PSZ predominantly consists of volcanic rock including Miocene tuffs and Tertiary (Miocene) basalts, with Quaternary sediments that are largely sourced from the volcanic rocks (Figure 15). Previous studies of the regional tuffs provided ages and phenocryst assemblages of various formations and units which allowed identification and correlation of tuffs within the study area (Scott and Swadley, 1992; Best et al., 1993, 2013a, 2013b). Some units, such as Tkg, have many different mechanical or eruptive units within them, making phenocryst assemblage estimation in the field important because it may be the only differentiating characteristic between units.

Quaternary sediments of varying ages occur throughout the study area; they are alluvial and older alluvial sediments (Qa, Qo1, Qo2), alluvial fans (Qaf, Qrf), lacustrine deposits (Qal), and older weakly consolidated conglomerates (Qtc). Overall unit descriptions for these sedimentary units are significantly different (Plate 1), but all consist of volcanic detritus from the surrounding area.

Radiocarbon analysis was performed by Beta Analytic in order to acquire an accurate depositional date for an alluvial fan (Qaf) that is cut by the MLF. Evidence of this offset is supported by the more recent deposition of a resurgent fan (Qrf) that overlies the Qaf and is also offset by the MLF. Dating material from the Qrf was not possible due to its very young age and large clasts; however Qaf is a much thicker unit relative to Qrf and allowed for good samples to be collected for ^{14}C analysis. Sample 449 was collected at 30 cm (1 foot) below the fan surface and yielded an age of 9550-9495 cal yr BP (Fig. 16). The second sample, 450, was collected at

60 cm (2 feet) below the surface and yielded an age of 10245-10190 cal yr BP (Figure 17) (Appendix 3, table 1). These data suggest that movement along the central portion of the MLF occurred within the last ~9500 years, and thus, the MLF was active in the Holocene (Table 1, Grid 1).

Seven distinguishable tuffs were identified along the central MLF and western Delamar Lake fault (DLF), to the north. Kane Wash Tuff, Gregerson Basin Member is the youngest tuff and originated from the Kane Springs Wash caldera (KSW) (Scott et al., 1992) and has two distinct cooling units which are separated by about 1 million years. Tkg2 is the younger of the two cooling units with a $^{40}\text{Ar}^{39}\text{Ar}$ age of 15.17 ± 0.03 Ma whereas Tkg1 is older with an age of 15.94 ± 0.05 Ma determined by $^{40}\text{Ar}^{39}\text{Ar}$ dating of samples 385/386 and 388, respectively (Appendix 3, table 2,3) (Figures 18, 19) . The $^{40}\text{Ar}^{39}\text{Ar}$ dating on the Kane Springs Wash Gregerson Basin Member was reported by Best et al., (1993) and Scott et al. (1993) providing ages that range between 14.1 and 14.5 Ma (Figure 15). More recent $^{40}\text{Ar}^{39}\text{Ar}$ dating of the Gregerson Basin Member was completed by Price (2017) and Evans (2018) which revealed ages of 15.3 ± 0.09 Ma and 15.13 ± 0.42 Ma, respectively. New and compiled $^{40}\text{Ar}^{39}\text{Ar}$ dates collected from the youngest Kane Springs cooling unit from Price (2017), Evans (2018), and this study, have an average age of 15.2 Ma and a high correlation that may suggest these new, but older dates are a more accurate age for the youngest tuff within the PSZ.

Seven other tuff units which originated from the Central Nevada and Caliente caldera complexes (Best et al., 1993, 2013) (Figures 2) are exposed with varying thickness across the study area. Grapevine Springs Member (Tkv) (which lies stratigraphically below Tkg1) has a reported $^{40}\text{Ar}^{39}\text{Ar}$ age of 14.7 Ma and an average thickness of 10 m. This 14.7 Ma age for Grapevine Springs Member conflicts with more recent ages collected from the stratigraphically higher

Gregerson Basin Member. More $^{40}\text{Ar}^{39}\text{Ar}$ ages from the Grapevine Basin Member are required to determine a more accurate age for this subunit. Hiko Tuff (Th) is the thickest unit, has a $^{40}\text{Ar}^{39}\text{Ar}$ age of 18.6 Ma and an average thickness of 300 m across the study area. Harmony Hills Tuff (Thh) has a $^{40}\text{Ar}^{39}\text{Ar}$ age of 22.2 Ma and an average thickness of 100 m across the study area. The Bauers Tuff (Tcb) Member of the Condor Canyon Formation, and Leach Canyon Tuff (Tlc) have $^{40}\text{Ar}^{39}\text{Ar}$ ages of 22.7 and 23.8 Ma, respectively, and both have an average unit thickness of 100 m.

Two distinct basalts were identified within the study area. The younger basalt (Tb1) lies stratigraphically between two units within the Gregerson Basin Member, Tkg1 and Tkg2, while the older basalt (Tb2) lies stratigraphically below the Grapevine Spring Member, Tkv. As well as differences in stratigraphic position throughout the study area, in hand sample, Tb2 clearly contains larger phenocrysts, particularly plagioclase, than the younger Tb1.

Chapter 5

Structural Data

The study area is separated into three domains, A, B, and C, that are bound by the two main NE-striking left-lateral faults, the Delamar Lake and Maynard Lake fault zones (Figure 20). Domains are distinguished by major structural similarities and geographical area. They will be described in order from north to south. Refer to Appendix 1 for a full list of compaction foliation and fault data for each domain.

Domain A

Domain A is located north of the DLF zone, and is characterized by predominantly NNW-striking normal-oblique faults that cut Miocene tuffs and Tertiary (Miocene) basalts, and abut the DLF. Fault surfaces in domain A are not well preserved due to brecciation and weathering that has resulted in rare opportunities to collect strike and dip, and fault data. However, geometries of the faults can be determined by high precision mapping and calculations. Faults are primarily steeply dipping with alternating dip directions. The result of these alternating faults is 160 meters of stratigraphic offset created by repeating horst and grabens of older Th juxtaposed with younger Tkg1. Faults in the east of this domain are exposed within Th and have varying strikes ranging from NNE to N-S. Faults continue to the north of the mapped area where interactions with other structures, such as the Buckhorn fault, may be possible. On the south, buried beneath older alluvium, faults of this domain abut the left-lateral DLF. One rake of 45° SE was measured on an NW-striking normal fault with a dip of 74° NE providing supporting evidence for normal-oblique slip within this domain. The most westerly compaction foliation measurements within the domain revealed west-dipping beds with dips ranging from 33-25°. Compaction foliation to

the east becomes more east-west striking with dips ranging from 20-11° (Appendix Table 1, table 1) (Figure. 20 and 21).

Delamar Lake Fault

The Delamar Lake fault is a major sinistral NE-striking fault with two major fault strands. N-S-striking faults exposed in Miocene units about the DLF (Figure. 20). The Delamar Lake fault has a minimum of 1.41 km of apparent left slip based on offset of the Th-Tb1 contact. The primary fault strand is mostly buried beneath Quaternary sediments with one surface exposure that strikes 060°. The fault strands continue northeast beyond the mapped area where it continues into the Delamar Lake quadrangle, which has been mapped by Scott et al. (1993) (Figure 1, B). A secondary strand with similar strike cuts Miocene tuffs and basalt units, and also exhibits left-lateral offset. The secondary strand breaks away from the primary strand in the east and can be traced to where it terminates at a north-northeast-striking normal fault in the west of domain B. Fault data recovered from the DLF is lacking due to burial and brecciation except for one fault measurement with a strike and dip of 280°, 85°NE and a rake of 85°N. This strike is not parallel to the main fault strand; it could represent a minor fault splay.

Domain B

Domain B lies between the sinistral MLF and DLF zones, and consists of predominantly N-S-striking normal-oblique faults that cut Miocene tuffs and basalts. Faults across this domain dip steeply either east or west. In the north of the domain, Tcb and Tlc units are exposed due to a large amount of dip-slip produced by a buried N-S-striking normal fault. Both the northern and southern tips of the faults in this domain about the DLF and MLF, respectively. No evidence of Quaternary faulting was observed within this domain. Fresh unweathered fault exposures with

slickenlines are common. There were nine rakes measured in domain B: 45° S, 90° S, 36° E, 32° NE, 44° NE, 90° SE, 75° NE, and 85° E (Appendix 1, table 2) (Figures 20, 21). These values indicate both oblique and dip-slip.

Compaction foliation measurements collected throughout domain B generally dip east-northeast with dips ranging from 18-30°. Some variation in strike can be observed in the east of the domain where Th units are heavily faulted and to the south where extensive brecciation is common.

Maynard Lake Fault

Four main strands of the MLF zone are exposed within the study area. The fault strands strike primarily NE showing both strike-slip to the NE of the study area (Figure 6) and normal-left offset in the SW of the study area (Figure 8). The MLF has a minimum of ~10 km of apparent left-lateral offset that can be measured on Scott et al.'s (1993) geologic map of the Delamar Lake quadrangle (Figure 1, B). Three of the faults mapped (1036, 1037 and 444) cut Quaternary units and the rest are exposed cutting Miocene volcanic rocks (Figure 20) (Appendix 1, table 3). The MLF continues to the NE into the Delamar 3 NW and Delamar Lake quadrangles for at least nine km (Scott et al., 1990, 1993) (Figure 1, B). Offset drainage patterns are observable from satellite and field observations along faults 1036 and 1037. Fault 444 has a measurable normal fault exposure that cuts Quaternary units that has a strike and dip of 220°, 85°NW (Figures 6, 21) (Appendix 1, table 3). Other faults with similar NE strikes cut Miocene volcanic rocks and have dips ranging from 40-86°.

Dip directions in this domain vary, but commonly are NW. Older Quaternary alluvium bedding measurements in the east and west of the domain strike NNE and dip west 13-15°W. Compaction foliation strikes range widely across the domain with steeper dips in the north and gentler dips in the south.

An open syncline along the eastern portion of the MLF zone within the study area folds Miocene tuffs (Plates 1 and 2) (Figure 22). The plunge and trend of the fold axis are 18° , 098° . The interlimb angle is 137° , which is a gentle fold. Nine compaction foliation measurements were used to calculate the dimensions of the structure which previously was partially mapped by Scott et al. (1993) in the Delamar 3 NW quadrangle. Five compaction foliation measurements were collected from the northern limb which has an average dip of $\sim 24^{\circ}$ S. Four measurements were collected from the southern limb which has a steeper dip of $\sim 40^{\circ}$ N.

Faults that offset Quaternary units

Within the study area, multiple fault strands within the MLF zone offset Quaternary units, including two left-lateral and one normal. The left-lateral faults are right-stepping which can be observed via map view or by satellite (Figure 6). Although evidence of scarp development is too subtle to identify even by ground mapping, offset drainage patterns between and to the SE of the faults strands clearly indicate Quaternary movement along these faults. Evidence to support the right-step is indicated by the northern-most sinistral fault which terminates to the NE within the Quaternary alluvium, while the southern sinistral fault strand continues to the NE through previously mapped areas (Scott et al., 1990, 1993) (Figure 1, B). Uplifted older Quaternary units between these faults and the exposed rocks that border the shear zone, indicate a zone of transpression (Plates 1, 2)

Vertical offset of Tertiary conglomerate resulted in production of a young Quaternary resurgent fan in the southwestern study area. This vertical offset indicates a change in slip from left-lateral to more oblique from NE to SW (Figure 8). Also to the SW, south of the fault, regional geology

can be observed to have a greater elevation than that to the NE, further supporting large amounts of oblique slip as we move SW.

Domain C

Domain C, located south of the MLF, is characterized by predominantly NNE- to NNW-striking normal faults and a gentle NNW-trending syncline which folds Miocene tuff and basalt (Plates 1, 2). Stratigraphic offset in domain C is small compared to domains A and B, ranging from a few to tens of meters where lower lithic Tkg1 (Tkl) is exposed. Many of the faults in this domain are exposed within Tkg1 which is extremely thick here compared to the rest of the mapped area making offset difficult to determine. Faults in this domain are predominantly steeply dipping and abut the MLF zone in the north of the domain. Two rakes were measured near the center of the domain on NNW- and NW-striking faults with dips of 50° and 90° , and rakes of 90° and 20° NW, respectively (Appendix 1, table 4) (Figures 20, 21).

Compaction foliation was measured on either side of the synclinal axis with dips on the west limb ranging from 5° - 27° east; measurements collected on the east limb of the fold ranged from 26° - 28° west. The strikes on each limb are predominantly NNW. The plunge and trend of the fold axis are 4° , 169° . The interlimb angle is 141° , a gentle fold (Figure 22).

Chapter 6

Structural Discussion

Left-lateral slip along the MLF and DLF had previously been previously documented within the study area (Tschanz and Pampeyan, 1970; Axen et al., 1993), but little was known of the fault and fold geometries, structural associations or structural interactions. Miocene deformation, Quaternary faults and syncline production are analyzed here to better understand the structural history and development of the study area.

The study area is composed of multiple faults and folds which formed and were active synchronously during the Miocene and/or Quaternary. Strike-slip faults separate three structural domains of normal- and oblique-slip faults that were active since emplacement of the Kane Wash Tuff at ~15 Ma. The predominantly N-S striking normal and oblique faults abut the two main strike-slip zones: the left-lateral DLF in the north and the more prominent MLF zone in the south. The MLF zone includes two major right-stepping fault strands with an area of transpression between them which was active as recently as the Quaternary. South of the MLF, a N-S striking normal fault produced drag resulting in a gentle syncline.

Maynard Lake Fault and Delamar Lake Fault as transfer faults

Transfer zones develop between two or more regions of differing deformational style and rate and consist of multiple transfer faults. Transfer faults are most commonly strike or oblique slip and trend parallel to the extension direction (Faulds and Varga, 1998). Map data collected shows different numbers and geometries of faults north and south of both the MLF and DLF suggesting that they are transfer faults. The transfer zone is consistent with fault strikes which are parallel to

the extension direction as recorded by Kreemer et al. (2010) using GPS stations which measured the current extension direction and slip rates along the zone. A larger amount of strain was recorded across the PSZ to the north within the NBR vs. less in the CBR (Sonder and Jones, 1999; Kreemer et al., 2010). In the case of the MLF and DLF, multiple generally N-S-striking normal faults transfer strain to these left-lateral systems from the north and south of the transfer faults. Previous research along the Arrowhead Mine fault and the Buckhorn fault suggest that these faults are transfer faults within the PSZ, and together are interpreted to form a transfer zone (Price, 2017; Evans, 2018).

The DLF does not have identifiable step-over faults, but two oblique fault strands that strike parallel to extension direction were mapped (Plate 1). I conclude that the DLF is a transfer fault resulting from differences in strain rates, distribution or amount produced by the faults between the NE portion of the Buckhorn fault and the MLF to the south. The MLF zone is also a zone of slip transfer from the north and south but unlike the DLF, there is evidence of Quaternary deformation along the zone.

Step-over along the Maynard Lake Fault

Step-over structures are common along transfer zones between overlapping fault segments and have previously been well documented around the world (Faulds and Varga, 1998; Lettis et al. 2002; Oglesby, 2005) (Figure 5). It is important to identify such structures within active zones of seismicity to better evaluate locations along faults that have a greater probability of allowing slip to propagate during an earthquake.

Along the central portion of the MLF, within the study area, overlapping, left-lateral, right-stepping fault strands create a zone of transpression (Plate 2 cross-section B) (Figure 6).

Surface mapping, cross-section and construction development across the MLF suggest multiple

reverse faults which together produce a positive flower structure between these two overlapping fault strands.

Calculation of the magnitude of an earthquake includes factors such as fault geometry, depth of and location of nucleation along fault strike, and type of fault (reverse, normal, strike-slip, or oblique) (Lettis et al. 2002; Oglesby, 2005). The geometry along the central portion of the MLF plays a large role in how an earthquake along this zone could either propagate or be arrested. Should an earthquake nucleate along either fault strand within the study area, the likelihood of the earthquake jumping from one fault strand to the other and continuing to propagate down a second fault segment depends on the step-over geometry. According to Oglesby (2005), the reverse faults that make up the transpressional flower structure will prevent earthquake propagation across the zone. Propagation along the central portion of the MLF would be more likely if the earthquake nucleated at the zone of transpression, the step-over. If the nucleation point was on a reverse fault within the step-over, the earthquake could propagate along either or both adjacent overlapping fault segments resulting in a greater earthquake magnitude (Oglesby, 2005) (Figure 6). From this point the earthquake may propagate to either/both overlapping fault segments, resulting in a larger magnitude earthquake than that which nucleated at the site of the reverse fault producing the step-over (Oglesby, 2005) (Figure 6).

Implications regarding possible future rupture along the MLF

The 36 km long MLF lies in close proximity to populated areas and extensive infrastructure (Las Vegas metropolitan area and Alamo). Consequently it is important to determine whether earthquakes are possible that may be felt in the populated areas. Calculations used to estimate earthquake magnitude require a surface rupture length. Length measurements were taken along strike of the MLF both along the entire known length of the fault and along fault segments.

Restraining bends as previously discussed are points along the fault zone where earthquakes may be arrested, so possibilities for earthquake magnitude were calculated for segments. Lengths of three fault segments were measured. The segments are separated by two possible restraining bends (Figure 1, B). Equations from Wells and Coppersmith (1994) ($M = 5.08 + 1.16 \log(\text{SRL})$ (where SRL is surface rupture length), or maximum displacement $M = 6.69 + 0.74 \log(\text{MD})$ (where MD is maximum displacement)), the updated version of the same equation by Hanks and Bakun (2008) ($M = \log A + 3.98 \pm 0.03$, where A (fault area) is $\leq 537 \text{ km}^2$ and $M = 4/3 \log A + 3.07 \pm 0.04$, where $A > 537 \text{ km}^2$) for earthquakes with magnitudes >7 , and Anderson et al. (1996, 2017) ($M_w = 5.12 + 1.16 \log L - 0.20 \log S$, that incorporates L (length in km), and S (slip rate mm/yr)) were utilized to calculate magnitude.

The entire fault and segment lengths were used as surface rupture lengths (SRL). The central segment was not divided at the step-over because the geometry is known, and for this study, only worst case scenarios will be calculated for moment magnitude. I assumed a focal depth of 10 km for Hanks and Bakun (2008), and a slip rate of 1.8mm/yr (Appendix 4, table 1). The assumption of a 10 km focal depth along the MLF is achieved by taking average nearby earthquake depth data provided by the USGS Quaternary Fault and Fold Database (U.S. Geological Survey and Nevada Bureau of Mines and Geology, 2006). A slip rate of less than 1.8mm/yr was provided by the Kreemer et al. 2010, providing a third set of possible results for magnitude across the MLF. Results from these calculations were fairly similar across the length of the zone and among the three calculations, producing moment magnitudes ranging from $M \sim 5.9$ on the shortest segment in the NE, to $M 6.8$ for the total length of the known fault zone (Appendix 4, table 1).

Syncline

Fault and fold data collected south of the MLF suggest a gentle syncline with an axial plane parallel to a N-striking normal fault. Map data collected across the fold suggest a single syncline, not an anticline-syncline pair as suggested by past research (Jayko, 2007). N-striking and E-dipping compaction foliations along the west limb of the fold are similar in strike and opposite to dip data collected east of the syncline (Plate 1). Two ways to produce folds near a normal fault are fault propagation and drag. Fault-propagation folds commonly produce anticline-syncline pair geometries between the hanging wall flat and the footwall flat due to an increase in the angle of fault dip along the footwall ramp. The lack of an anticline excludes fault propagation folding. In the case of this syncline, a drag-fold interpretation is more likely. Drag folds form where displacement changes along a fault. Gently dipping limbs on the syncline produce low angles from horizontal relative to the fault plane and are consistent with normal drag (Grasemann et al., 2005) (plate 2 cross-section D). I suggest that this syncline developed due to the propagation of a N-striking, E-dipping normal fault that experienced a reduction in slip as it continued north and ultimately transfers its strain to the MLF (Plate 2) (Figure 20). The core of the syncline is now filled with Quaternary sediments that also overlap the N-striking fault.

A gentle south-plunging drag fold exposed in Miocene volcanic rocks produced a basin that is now filled with Quaternary deposits south of the MLF. A N-striking normal fault has a decrease in displacement as it approaches the MLF to the north which caused drag folding.

Chapter 7

Regional Interpretation

Mesozoic Deformation

The MLF was suggested by Jayko (1990) to have originally developed as a transfer zone between the Mesozoic Gass Peak thrust to the south of the MLF and the Eastern Pahrana gat syncline to the north during the Sevier orogeny. Taylor et al. (2000) suggest that the Gass Peak thrust is cut and offset by the PSZ and that shortening continued to the north along the Pahrana gat thrust, East-Pahrana gat fault, Mount Irish thrust, and farther north, the Golden Gate thrust. Together these latter structures make up a large portion of the Jurassic – Cretaceous central Nevada thrust belt, a part of the Sevier orogenic belt. Deformation along the MLF may have begun during deformation of the central Nevada thrust belt, but no rocks older than 23.8 Ma are exposed in the map area, and thus, early Mesozoic deformation will not be examined based on the new data.

The Maynard Lake fault and the Caliente Enterprise zone are distinct zones

A comparison of previous maps and inspection of aerial imagery of the northeastern MLF and southwestern CEZ suggests that a soft linkage of the MLF and the CEZ is possible (Tschanz and Pampeyan, 1970; Jayko, 1990; Axen, 1998). Lack of data, continuous mapped faults or surface fault interactions between the MLF and CEZ, result in little evidence to support a hard linkage between the two zones. Differences in regional stress directions, deformational style, magnitude of offset, and extensional timing all suggest that the CEZ does not transfer strain directly to the PSZ. Soft linkage is possible because both zones are left-lateral, lie along strike of each other and the proximal tips of each zone are relatively close to each other. The PSZ and CEZ are

distinct zones but may have similar regional deformational driving forces behind them. Previous map data and research conducted within the CEZ suggest that most of the deformation ended during the Late Miocene, so the soft linkage maybe pre Quaternary (Tschanz and Pampeyan, 1970; Axen, 1998).

Transfer Zone

Transfer zones are distinct zones of strike- and oblique- slip faults that strike parallel to the extension direction and facilitate a transfer of strain from separately extending surrounding regions (Faulds and Varga, 1998). The northern and southern boundaries of the PSZ are both characterized by left-lateral faults: the Arrowhead Mine fault (Tschanz and Pampeyan, 1970; Jayko, 2007; Evans, 2018) and the MLF, respectively. Generally N-striking faults to the north and south of the PSZ abut and produce acute oblique angles to shear zone bounding faults such as the Arrowhead Mine fault and MLF. One N-striking fault which abuts the Arrowhead Mine fault along the southwestern portion of the fault was mapped by Evans (2018). Multiple N-striking normal faults south of the PSZ abut the MLF in the same map area. N-striking faults were also mapped along the SW-portion of the MLF (Muhammad, 2016), along the NE-portion (Scott et al., 1990), and in this research along the central portion, as well as on various regional maps (Tschanz and Pampeyan, 1970; Jayko, 2007). The abutting of these N-striking faults to the entire MLF support the transfer fault interpretation.

To the south of the MLF, multiple predominantly N-striking normal faults that are active during the Quaternary include (from east to west); the Coyote Springs fault, Sheep Range fault and the Sheep Basin fault (Figure 3). Work conducted SW along the MLF suggests the MLF terminates NE of the Desert Hills (Mohammad, 2016), with possible fault interactions with the Sheep Basin fault (U.S. Geological Survey and Nevada Bureau of Mines and Geology, 2006). The Coyote

Springs fault (Scott et al., 1990) also may transfer strain to the MLF through a subparallel strike-slip fault. Together these faults create a region of E-W extension south of the MLF more recent than extensional structures to the north including the Highland and Stampede detachments that were active during the Miocene and Paleogene or Late Mesozoic, respectively (Taylor and Bartley, 1992; Hudson et al., 1998) (Figure 3). Quaternary faults to the north of the PSZ, such as the Dry Lake fault, generally end distinctly north of this strike-slip system (U.S. Geological Survey and Nevada Bureau of Mines and Geology, 2006) (Figure 3). Thus, the PSZ is a transfer zone that accommodates these differences in regional Quaternary deformation in the form of ENE-striking sinistral faults including the MLF.

Chapter 8

Conclusions

Research along the central MLF within the PSZ provided explanations for the structural development and the regional history of the zone. Regional strain transfer resulted in an active transfer zone that consists of three significant NE-striking sinistral faults including the MLF that has recorded movement within the last ~10,000 years. The MLF is capable of significant magnitude earthquakes that could pose a ground shaking hazard to Las Vegas and other proximal populated areas.

Structural Explanations

1. The MLF is a transfer fault that transfers strain from surrounding N-striking normal fault systems resulting in left-lateral and oblique shear within the PSZ. It is clear that the MLF was active after ~15.2 Ma because it and related faults cut the youngest unit, the Kane Wash Tuff.
2. A gentle south-plunging drag fold exposed in Miocene volcanic rocks produced a basin that is now filled with Quaternary deposits south of the MLF. A N-striking normal fault has a decrease in displacement as it approaches the MLF to the north which caused drag folding.
3. The Delamar Lake fault is a transfer fault that conveyed strain from the normal faults to the south, and an area of extension to the north of the mapped area and south of the Buckhorn fault.
4. Fault strands mapped along the MLF exhibit drainage offsets within Quaternary older alluvial units. Minimal fault scarp development along these strands suggests a dominantly strike-slip sense of movement along the central segment of the MLF.

5. A resurgent fan induced by normal-oblique movement along the MLF occurred within the last ~10,000 years as suggested by radiocarbon sediment analysis of the offset Qaf. Displacement along this portion of the fault suggests that the strike-slip sense of movement becomes oblique with a small normal component in and to the SW of the study area.

6. Map data and cross-sections reveal a zone of transpression between left-lateral, right-stepping overlapping fault strands along the central portion of the MLF. This transpressional step-over structure could arrest an earthquake should nucleation occur along either fault strand.

7. Moment magnitude calculations using total fault length (km), fault segment length (km) and an assumption of a 10 km fault depth reveal possible moment magnitudes between 5.9 and 6.8, which are considered large enough to pose a ground shaking hazard to Las Vegas and other populated areas such as Alamo.

Regional

1. The MLF is the longest fault within the PSZ and forms the southern boundary of the PSZ.

Map data along the NE portion of the MLF does not support a hard linkage between the MLF and faults within the CEZ. Although hard linkage cannot be confirmed, soft linkage between the zones is possible. Therefore I conclude that the PSZ and the CEZ are distinct zones along the subprovince boundary.

2. The PSZ is a transfer zone that accommodates differences in regional strain to the north and south of the NBR and CBR subprovince boundary. The transfer zone contains a system of left-lateral transfer faults including the Arrowhead Mine fault, Buckhorn fault, and the MLF, as well as the Delamar Lake fault. This transfer zone was active from at least ~15 Ma to the Holocene.

Figures

A.



B.

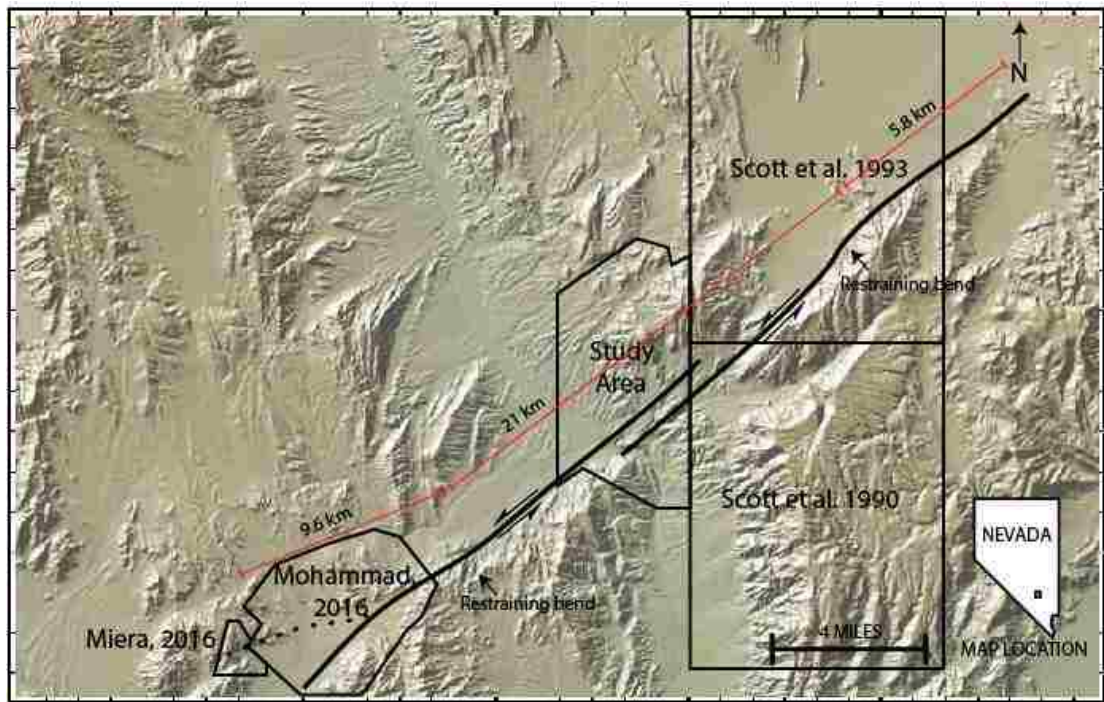


Figure 1 Faults and previous work.

A. Generalized map of the PSZ and the three main sinistral faults including the Arrowhead Mine fault, Buckhorn fault, and the Maynard Lake fault (black). Left-lateral Delamar Lake fault (DLF) (grey). Grey box represents location of (Figure 6). Fault geometries along the eastern AMF and BHF provided by Aaron Christianson and Becky Ely respectively (Ely et al., in progress).

B. Locations of previous geological maps and study area along the MLF (Scott et al. 1990 and 1993; Mohammad, 2016; Miera, 2016). Distances between restraining bends and their measured values are shown as red lines. General location of MLF indicated by black line. (Base map modified from GeoMapApp).

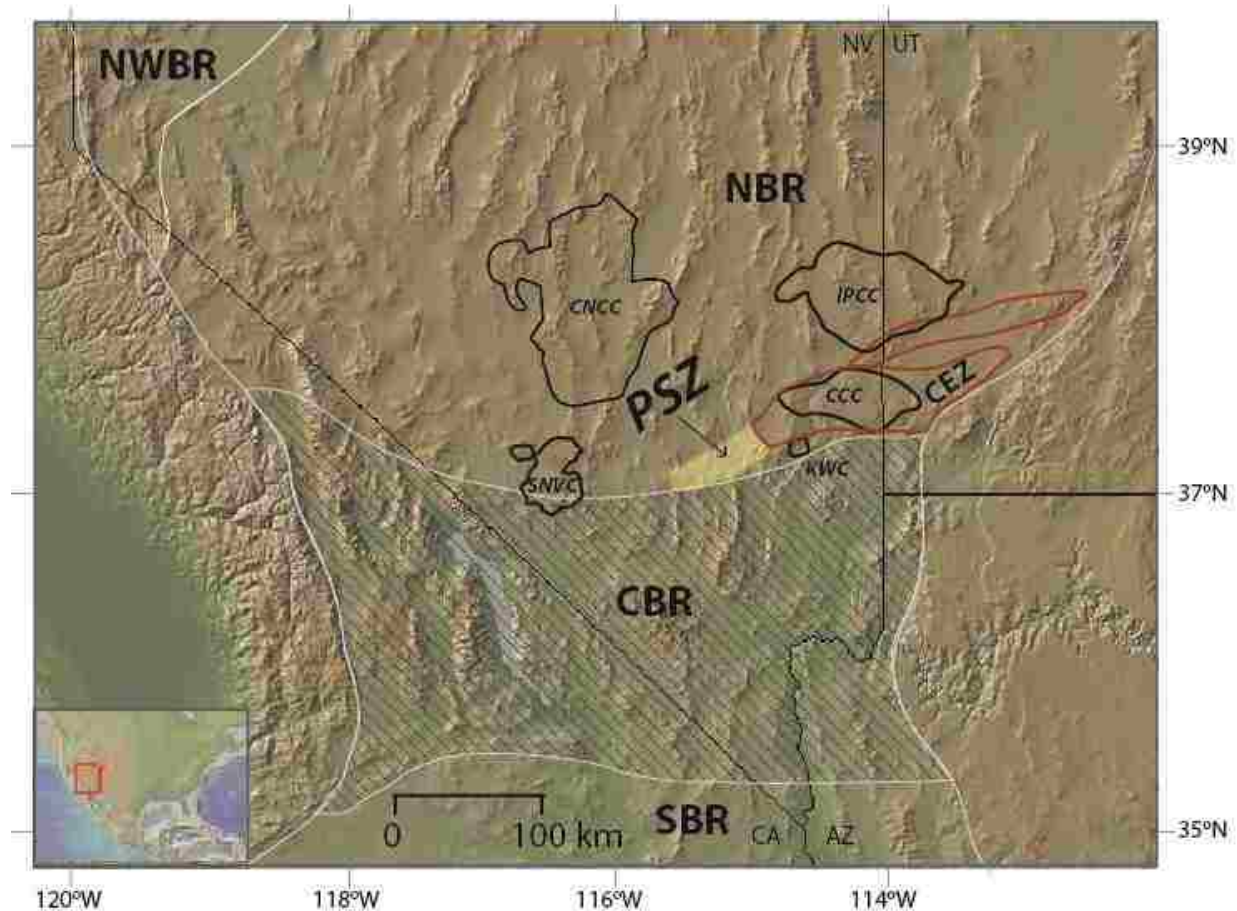


Figure 2 Basin and Range.

Map showing Northwest Basin and Range (NWBR), NBR, CBR and SBR sub-provinces outlined in white. Note the lower elevations of the basins (green) in the CBR and SBR in comparison to the higher basin elevations (tans) in the NBR. Caliente caldera complex (CCC), Central Nevada caldera complex (CNCC), Indian Peak caldera complex (IPCC), Kane Springs Wash caldera (KWC), and Southern Nevada volcanic complex (SNVC), are outlined in black. Pahrnagat Shear zone (PSZ) represented in yellow. Base map from Global Multi-Resolution Topography (GMRT) synthesis.

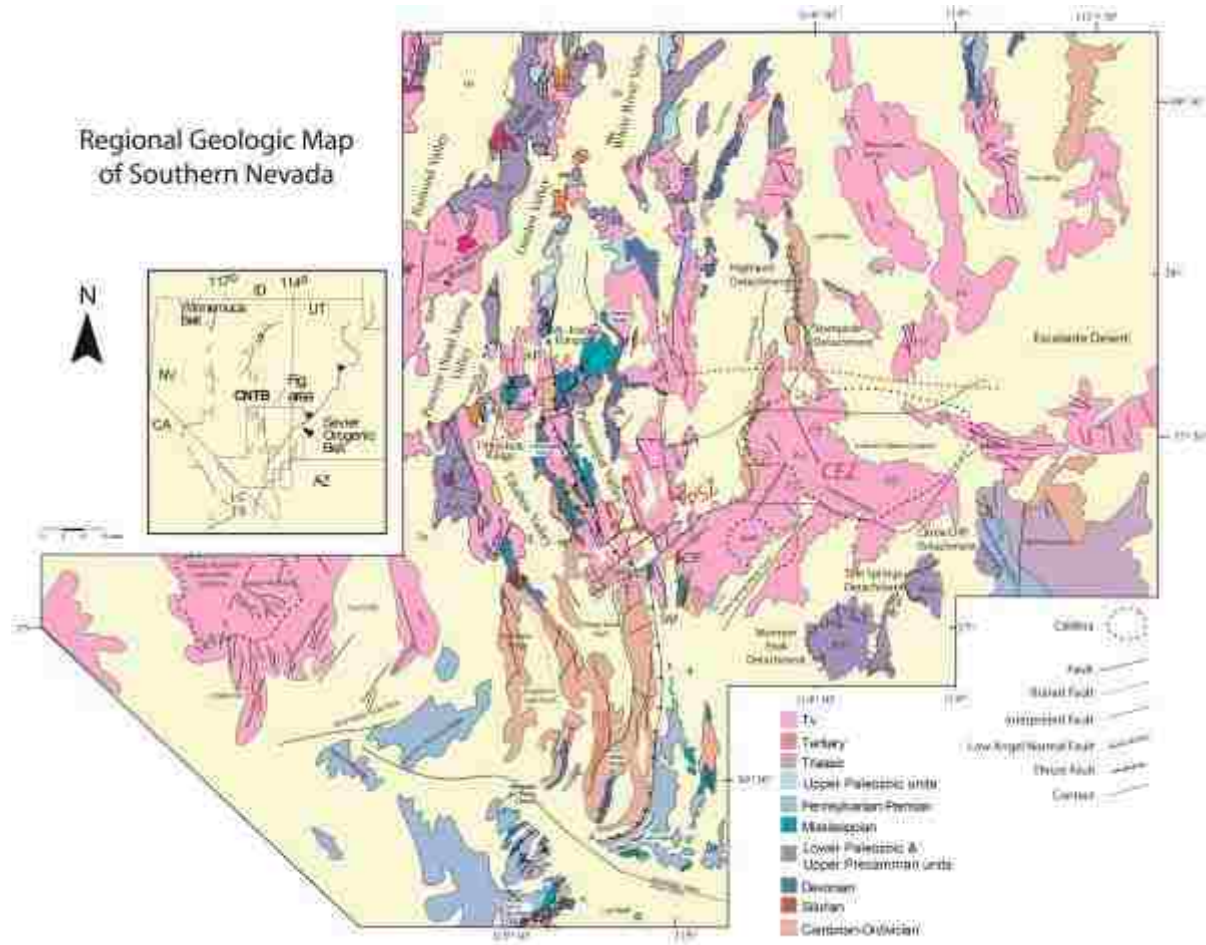


Figure 3 Regional geologic map

Regional geologic map of parts of southern Nevada and southwestern Utah. Items of interest include the Pahrnagat shear zone (PSZ) including the three major faults: Arrowhead Mine (AMF), Buckhorn (BF) and MLF; Caliente-Enterprise zone (CEZ); calderas (black dotted lines); Coyote Spring fault (CSF); Sheep Range fault (SRF); Kane Springs Wash fault; and detachment faults. Red dotted line represents general location of Timpahute lineament as described by Ekren et al. (1976). Modified from Price (2016) and Evans (2017).

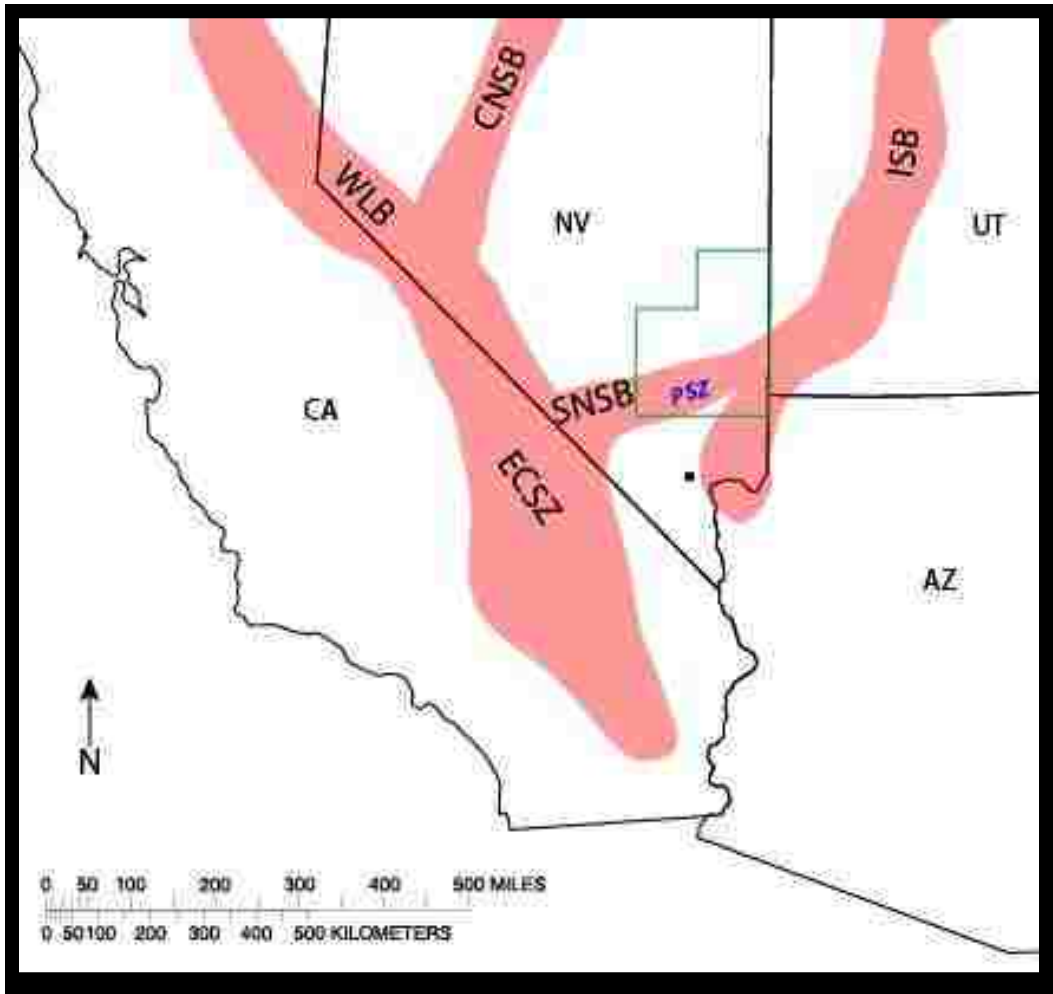


Figure 4 Seismic belts

Map of relevant seismic zones including the southern Nevada seismic belt (SNSB), Walker Lane seismic belt (WLB), central Nevada Seismic belt (CNSB), Eastern California shear zone (ECSZ), and the Intermountain seismic belt (ISB). Location of the PSZ is highlighted in blue. Black dot represents general location of Las Vegas and green polygon outlines the border of Lincoln County.

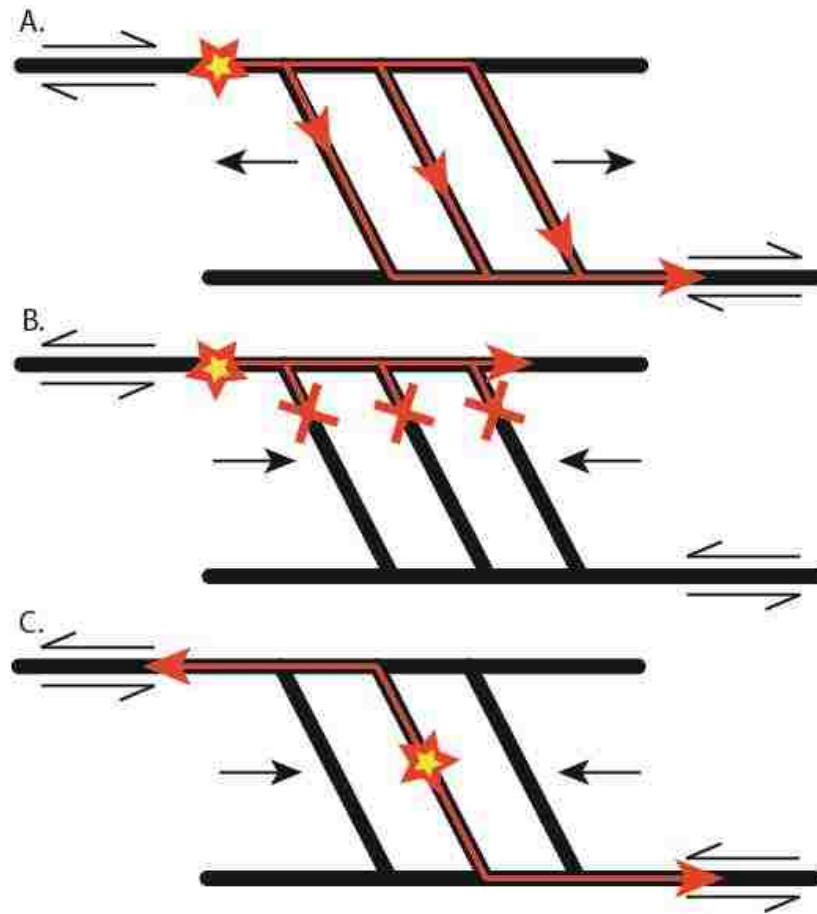


Figure 5 Step-over structures

Simplified diagram of step-over structures between two left-lateral right-stepping overlapping fault strands. A. Zone of transtension between fault strands allows for earthquake nucleation (star) and propagation (red lines with arrow) to jump from one fault strand to the other. B. Zone of transpression between fault strands causes earthquake propagation to terminate (red crosses) at reverse faults when nucleation site is on either fault strand. C. Zone of transpression between fault strands allows for earthquake propagation to one or both fault strands when nucleation site occurs at reverse faults.

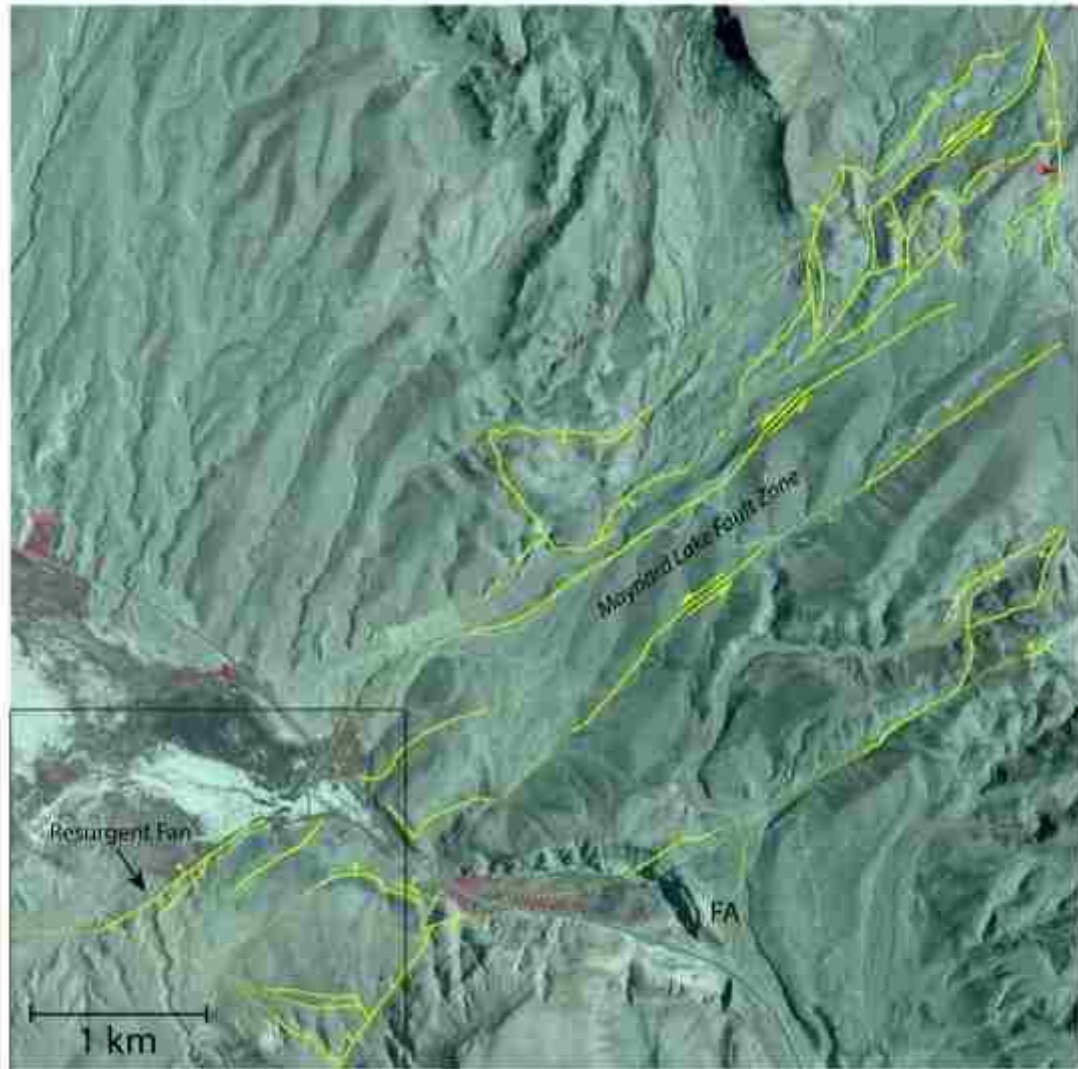


Figure 6 Maynard Lake fault strands

NAIP imagery of faults associated with the MLF zone within the study area. Yellow lines represent mapped faults. Black polygon outlines the location for Figure 7. $37^{\circ}12'31''\text{N}$ $115^{\circ}01'49''\text{W}$ (center of map). Red dotted line and arrow represent gentle fold along the MLF. "FA" represents that major normal fault within domain C.

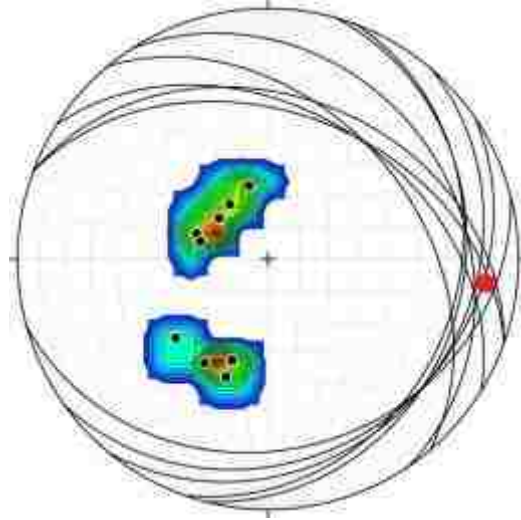


Figure 7 Stereographic projection of gentle fold along the Maynard Lake fault

Stereographic projection of gentle syncline located within the MLF zone in the eastern study area. Plunge and trend of fold axis is 18° , 098° . Interlimb angle is 137° . Fold axis indicated by red dot.

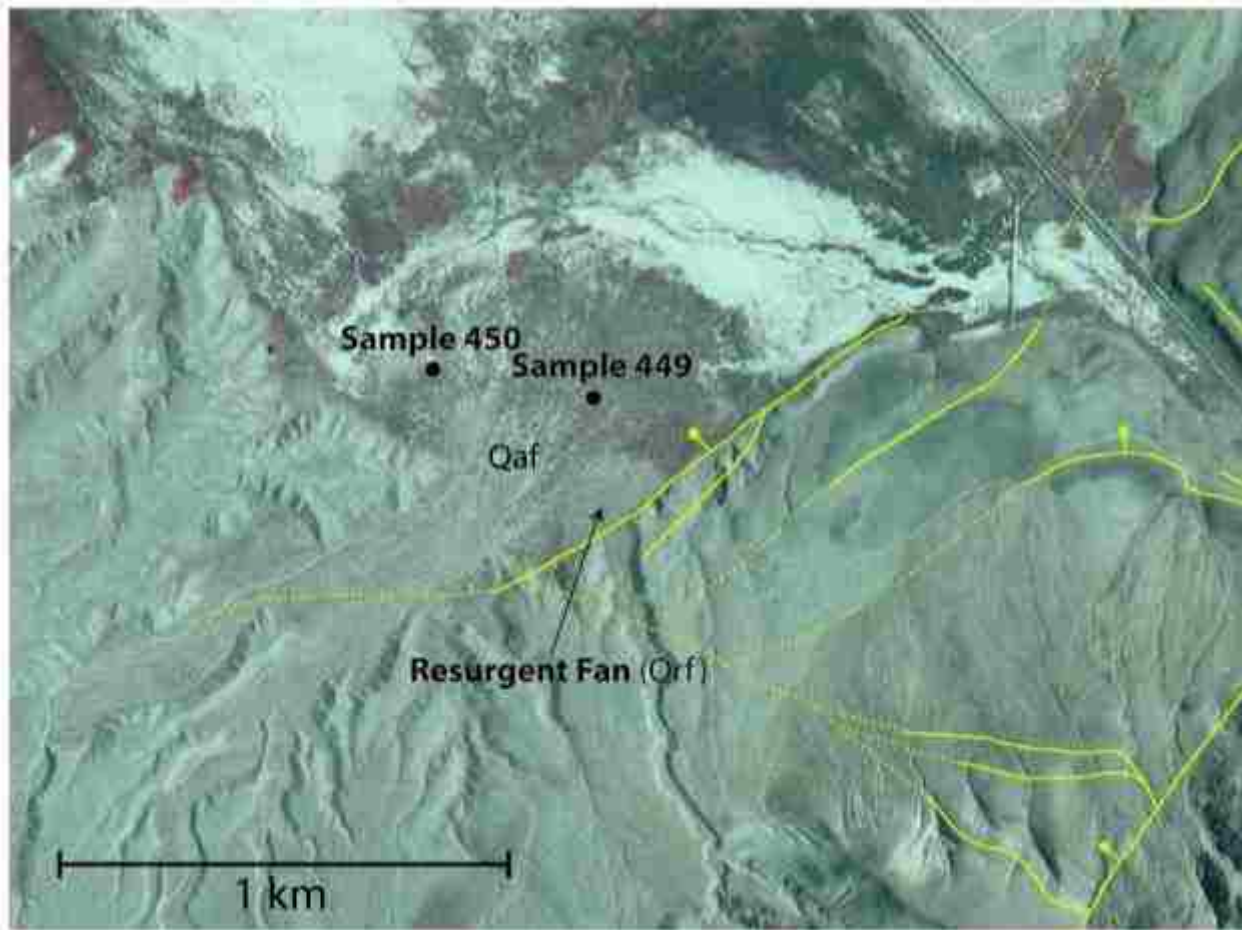


Figure 8 Resurgent fan

Alluvial fan (Qaf) with radiocarbon soil sample collection locations and younger resurgent fan produced as a result of offset along the MLF (yellow). Base map modified from orthoimagery. Yellow lines represent mapped faults. $37^{\circ}11'32\text{N } 115^{\circ}03'13\text{W}$ (center of resurgent fan)



Figure 9 Sediment sample 449 hole

Bulk sediment sample 449 collected at 30 cm (1 foot) below surface of alluvial fan (Qaf). Handle length is approximately 30 cm (1foot) from end of handle to base of trowel.



Figure 10 Sediment sample 450 hole

Bulk sediment sample 450 collected at 60 cm (2 foot) below surface of alluvial fan (Qaf). Handle length is approximately 30 cm (1 foot) from end of handle to base of trowel.



Figure 11 Sediment sample 449 bulk sediment

Figure 449 soil. Bulk sediment sample 449 before carbon extraction (picture provided by Beta Analytic).



Figure 12 Sediment sample 450 bulk sediment

Figure 450 soil. Bulk sediment sample 450 before carbon extraction (picture provided by Beta Analytic).



Figure 13 Sediment sample 449 carbon

Figure 449 carbon. Datable carbon extracted from bulk sediment sample 449 (picture provided by Beta Analytic).



Figure 14 Sediment sample 450 carbon

Figure 450 carbon. Datable carbon extracted from bulk sediment sample 450 (picture provided by Beta Analytic).

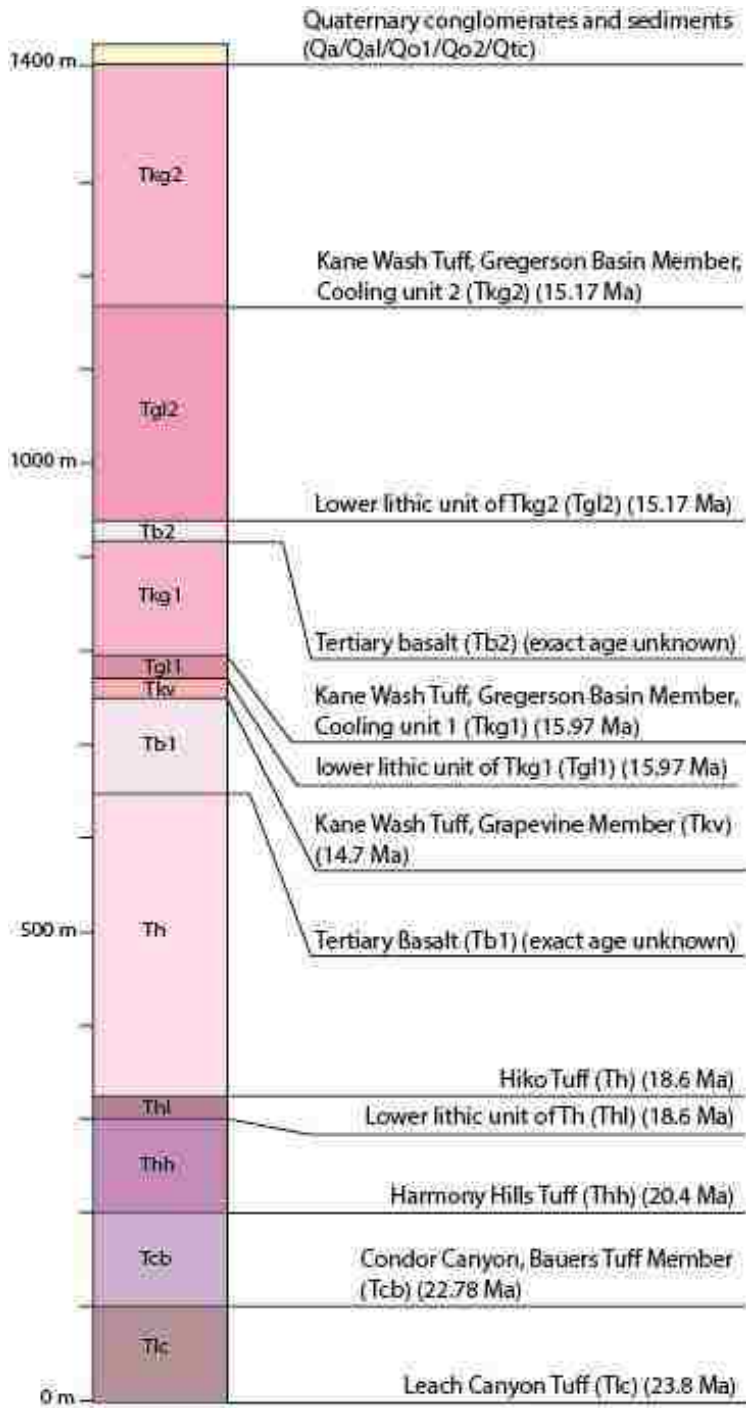


Figure 15 Stratigraphic column

Stratigraphic column of Oligocene, Miocene, and Quaternary units within the study area. Relative thicknesses of the units correlate to field map (Plate 1). Details for dates listed for Tkg1 and Tkg2 can be found in Appendix 2. All dates except for Gregerson Basin Member were

published by Best et al. (1993). Age of Grapevine Member is younger than new dates on Gregerson Basin Member, and thus is considered questionable.

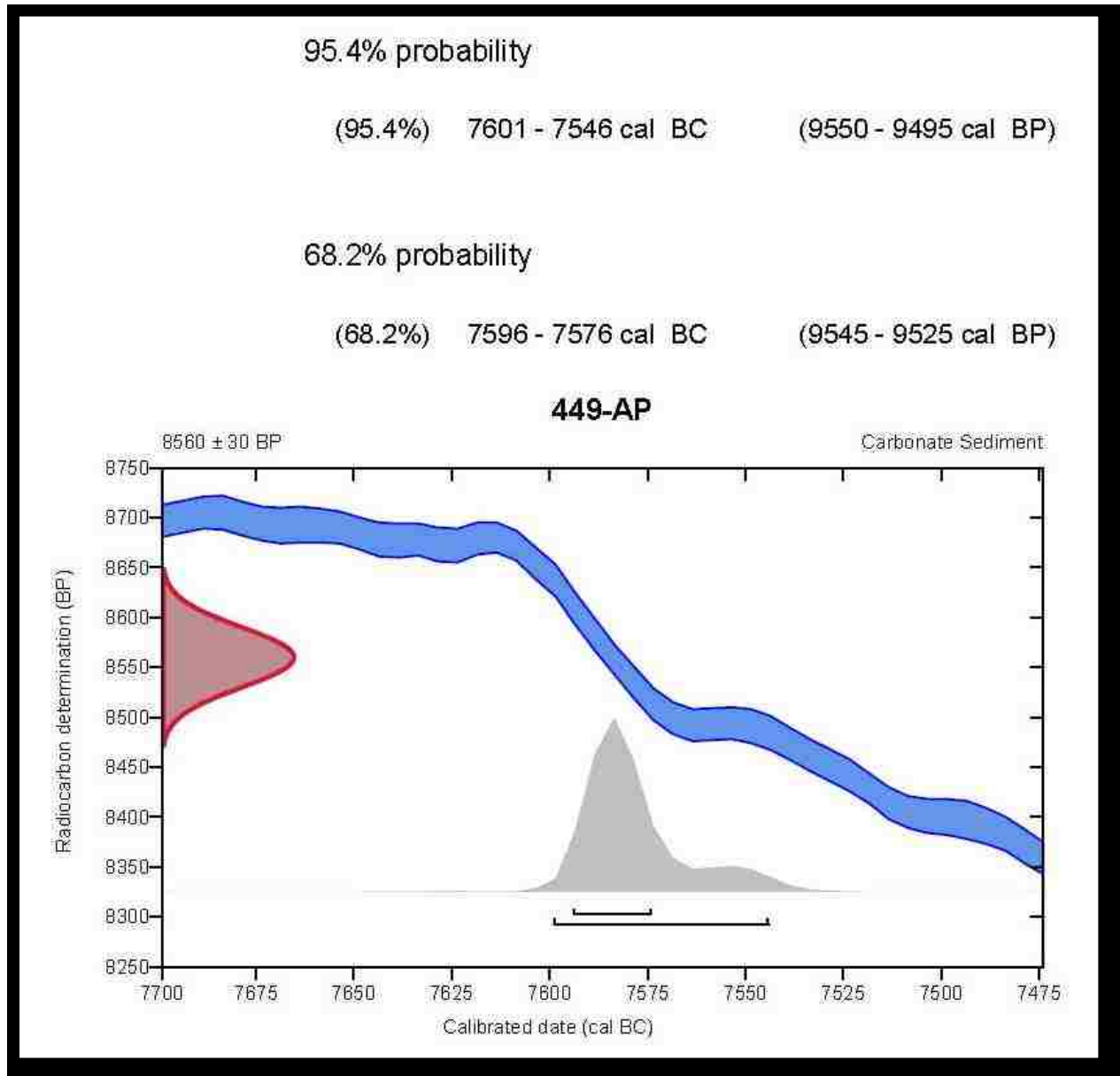


Figure 16 Sediment sample 449 radiocarbon data

Calibration of radiocarbon age to calendar years (high probability density range method (HPD): INTCAL13) for 449-AP. Blue line represents ^{14}C values collected from sample. Red graph represents 95.4% probability range in BP (before present, 1950). Grey graph represents both

95.4% and 68.2% probability ranges in calibrated years BC. Bars on grey graph represent standard deviation.

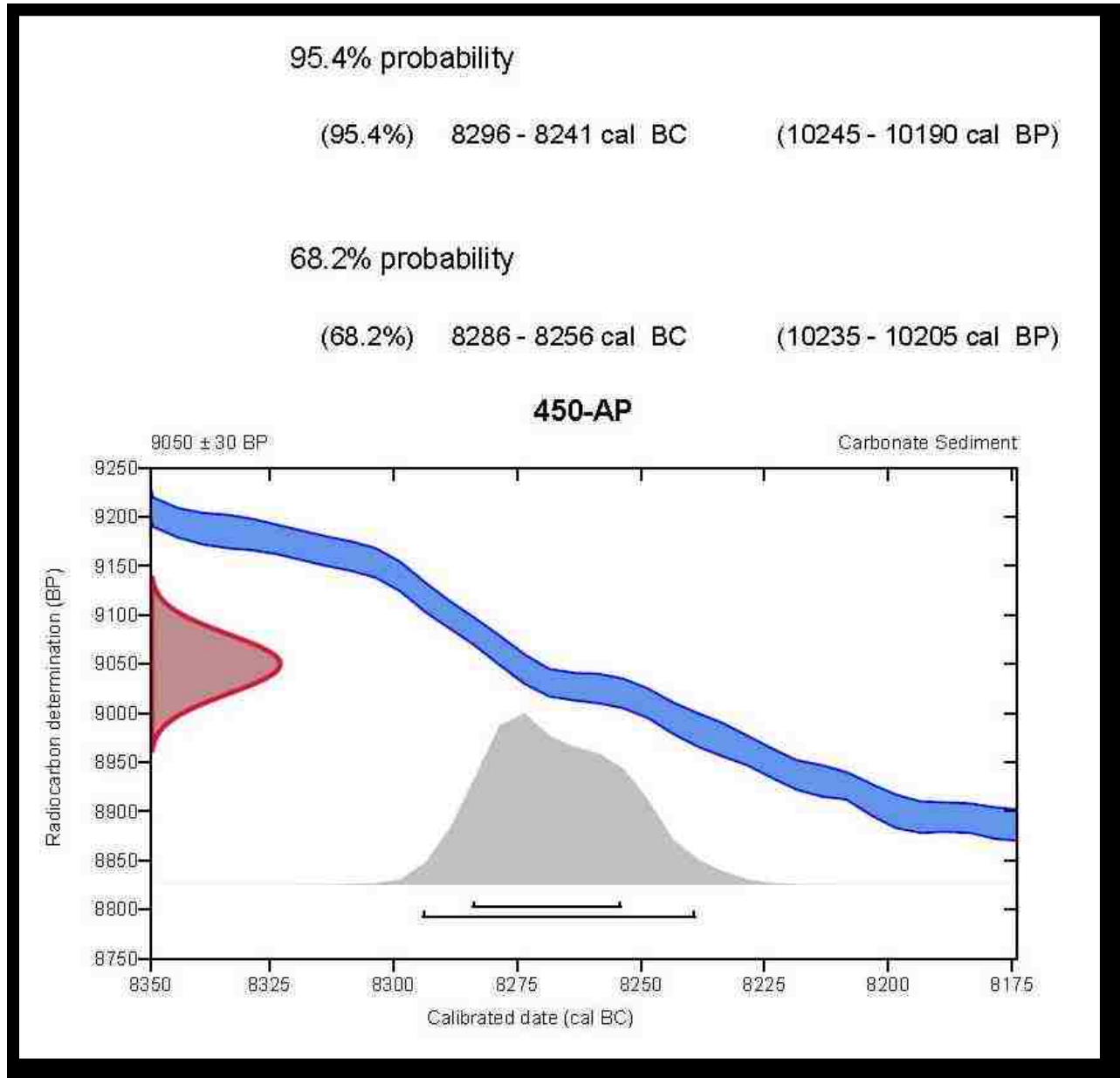


Figure 17 Sediment sample 450 radiocarbon data

450-ap Calibration of radiocarbon age to calendar years (high probability density range method (HPD): INTCAL13) for 450-AP. Blue line represents ¹⁴C values collected from sample. Red graph represents 95.4% probability range in BP (before present 1950). Grey graph represents both 95.4% and 68.2% probability ranges in years BC.

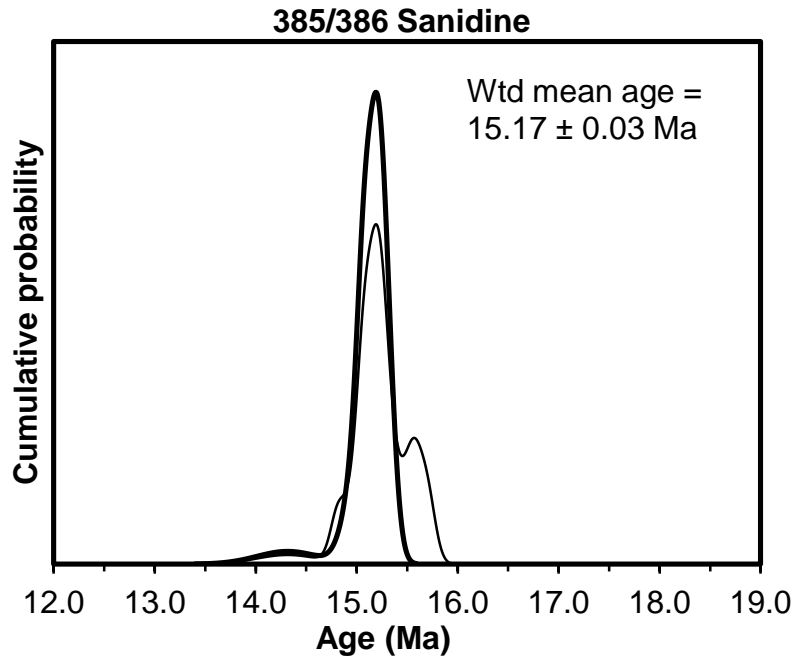


Figure 18 Sample 385/386 mean age

Probability graph showing the probability of the given age based on the samples measured. It shows the highest probability of the weighted mean age to be 15.17 ± 0.03 Ma.

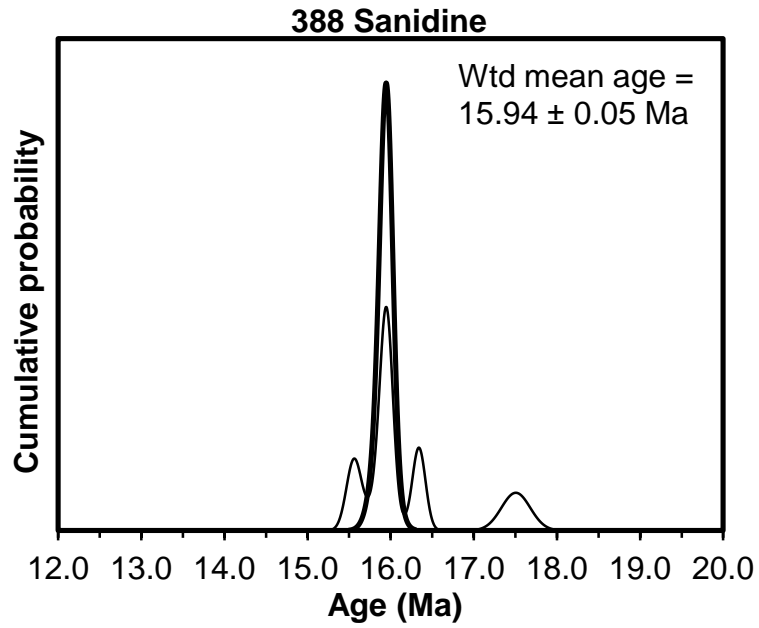


Figure 19 Sample 388 mean age

Probability graph showing the probability of the given age based on the samples measured. It shows the highest probability of the mean age to be 15.94 ± 0.05 Ma.

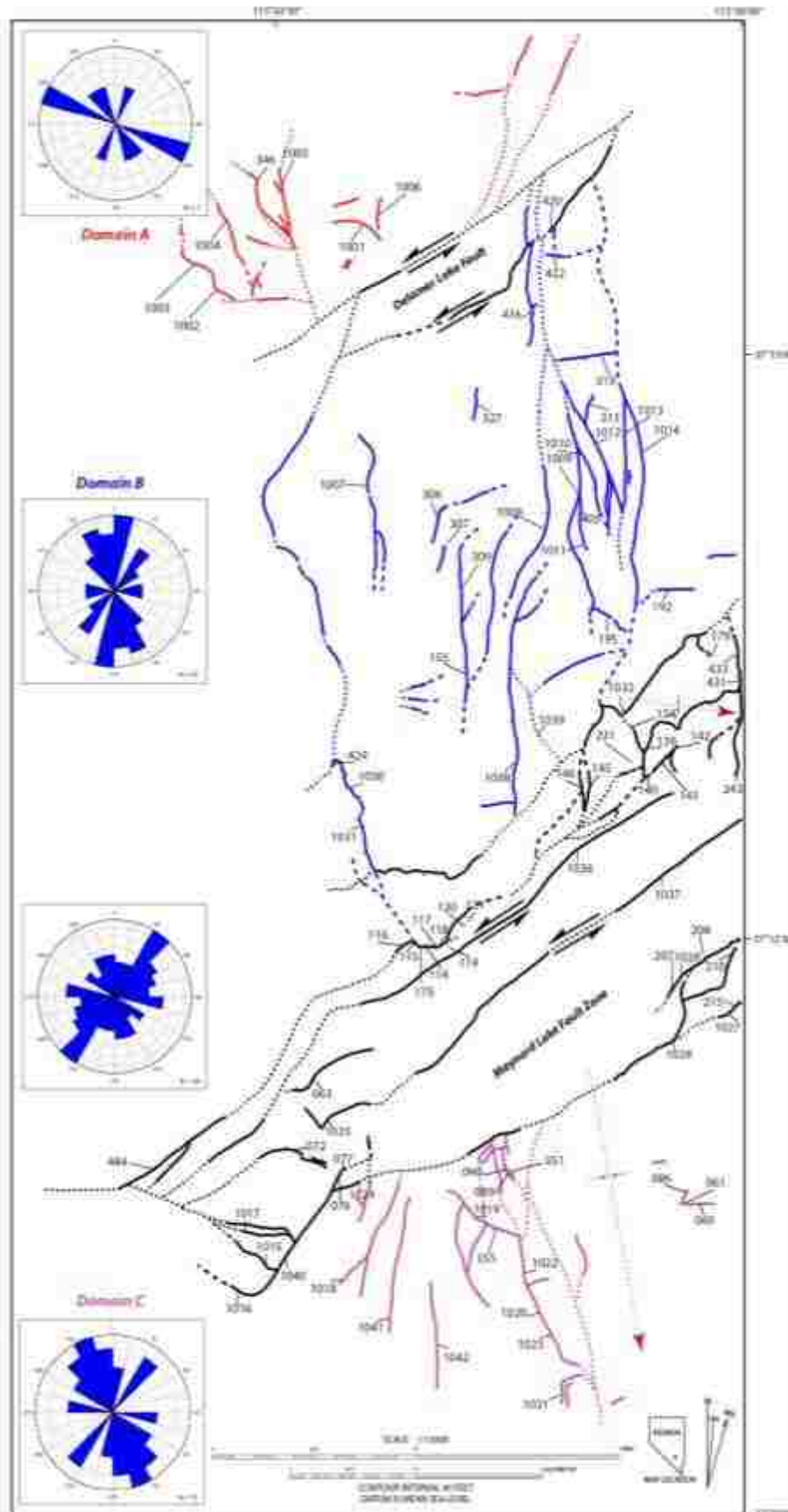


Figure 20 Fault map

Fault map structures are divided into three domains: Domain A (red), Domain B (blue), and Domain C (violet). Delamar Lake Fault zone and Maynard Lake Fault zone are shown in black. Fault identification number information is provided in Appendix 1. Rose diagrams for each domain are listed as so. The Maynard Lake fault rose diagram is unlabeled but adjacent to the fault zone.

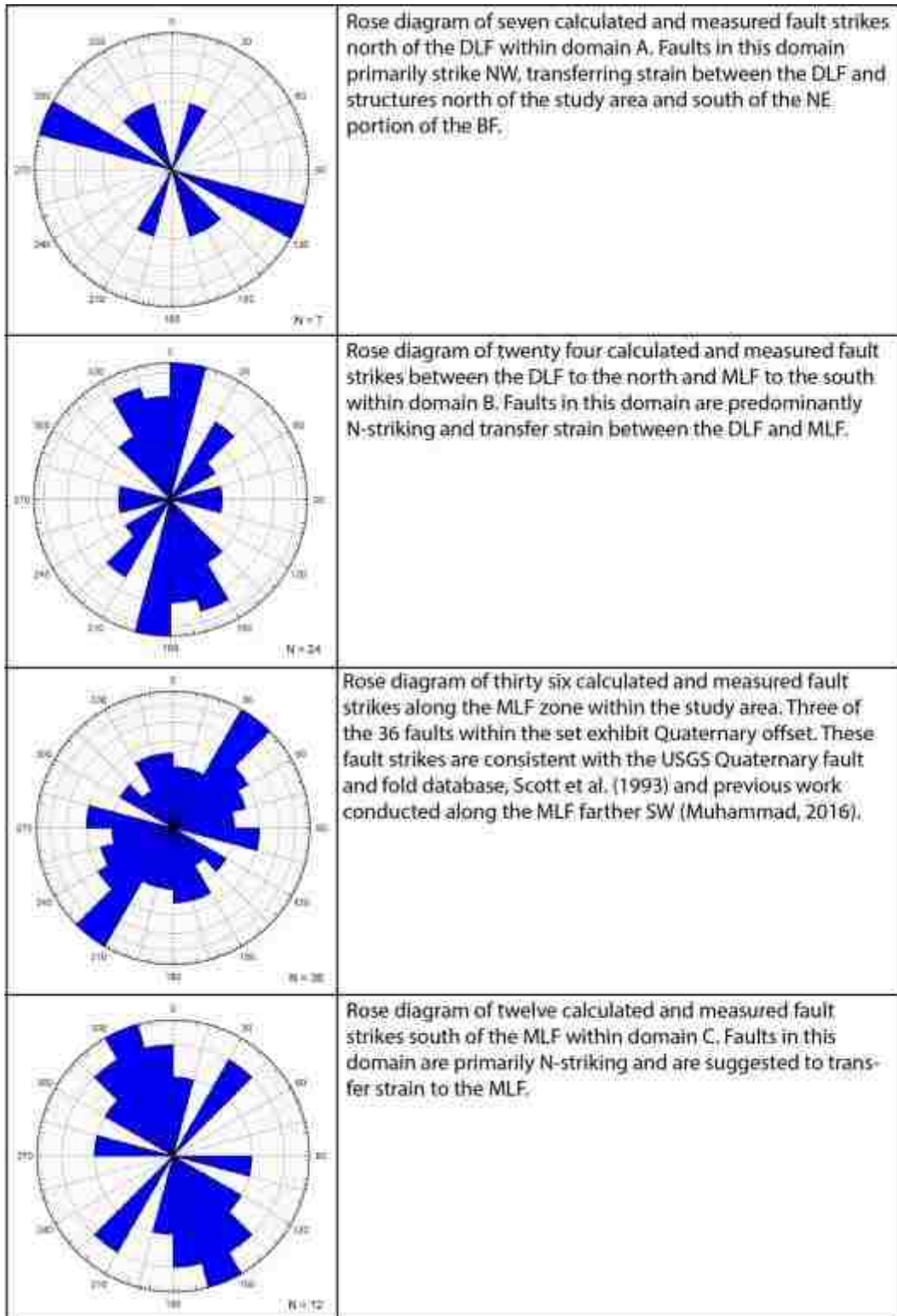


Figure 21 Rose diagrams

Domain locations of data for rose diagrams are shown on Fig. 20.

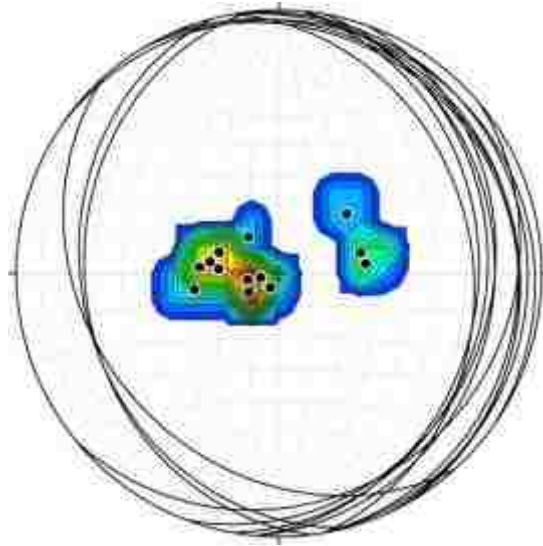


Figure 22 Stereographic projection domain C

Stereographic projection of gentle syncline located in domain C. Plunge and trend of fold axis is 4° , 169° . Interlimb angle is 144° .

Appendix 1

Table 1. Compaction foliation measurements collected in domain A

Domain A Data

Compaction Foliation Field Measurements:

Station #	Unit	Strike	Dip	Location	
341	Tkg	130	25	37.26056	-115.049
342	Tsg	11	6	37.26144	-115.048
345	Th	160	32	37.26089	-115.047
367	Th	185	33	37.25368	-115.048
370	Tkg	110	33	37.25402	-115.047
373	Tkg	85	11	37.25457	-115.044
375	Tkg	125	25	37.25775	-115.041
379	Th	65	20	37.25649	-115.035
380	Th	10	22	37.26027	-115.025
381	Th	245	12	37.25523	-115.029
383	Qo2	65	10	36.37744	-114.894

Measured faults:

Fault id.	Strike	Dip	Rake	Location	
346	297	74	45SE	37.26306	-115.045

Calculated faults:

Fault id.	Strike	Dip
1001	106	36
1002	299	6
1003	292	5
1004	156	67
1005	147	35
1006	29	37

Table 2. Compaction foliation measurements collected in domain B

Domain B Data

Compaction Foliation Field Measurements:

Station #	Unit	Strike	Dip	Location	
151	Tkg	5	10	37.22776	-115.017
154	Th	155	5	37.22522	-115.026
165	Th	80	25	37.2215	-115.026
166	Th	310	26	37.2215	-115.026
167	Th	210	20	37.21964	-115.026
168	Th	190	15	37.21915	-115.028
169	Th	140	10	37.21995	-115.029
170	Th	115	21	37.21643	-115.031
171	Th	70	10	37.21538	-115.033
173	Tkg	60	60	37.21935	-115.035
190	Th	150	25	37.23458	-115.004
196	Th	15	24	37.2311	-115.012
250	Th	25	85	37.223	-115.036
258	Qo	horizontal		37.23132	-115.03
262	Th	65	26	37.23591	-115.011
267	Th	240	20	37.24036	-115.013
269	Th	180	35	37.24025	-115.012
270	Th	65	5	37.24138	-115.011
271	Th	5	25	37.24165	-115.011
272	Th	100	23	37.24055	-115.011
275	Th	255	15	37.22077	-115.01
279	Th	350	31	37.23271	-115.018
287	Tkg	340	10	37.23447	-115.024
288	Tkg	355	40	37.2339	-115.026
291	Tkg	horizontal		37.23374	-115.027
292	Tkv	355	30	37.23457	-115.028
294	Tkv	300	25	37.23414	-115.028
295	B1	115	15	37.23349	-115.029
296	Th	60	15	37.23532	-115.03
297	Th	0	25	37.23601	-115.031
298	Tkv	340	10	37.23784	-115.031
301	Th	285	16	37.23884	-115.033
303	Tkv	345	15	37.2402	-115.031
304	Tkv	0	18	37.24064	-115.03

305	Tkv	45	25	37.23899	-115.029
306	Tkg	290	35	37.23488	-115.028
308	Tkg	278	26	37.23469	-115.026
310	Th	345	20	37.24496	-115.026
312	Th	345	25	37.24748	-115.012
313	Th	5	30	37.24732	-115.013
314	Th	5	18	37.24707	-115.014
315	Tkg	25	15	37.24783	-115.014
316	Th	165	65	37.24819	-115.014
317	Th	15	32	37.24903	-115.013
318	Th	350	20	37.24904	-115.014
319	Th	352	30	37.25074	-115.014
322	Th	250	15	37.24778	-115.021
325	Tkv	45	10	37.24702	-115.024
326	Tkv	345	18	37.24031	-115.025
382	Qo2	180	10	37.22301	-115.047
385	Tkg	30	22	37.22301	-115.016
399	Tcb	5	25	37.24744	-115.015
402	Tkg	190	10	37.24113	-115.012
403	Tkg	206	16	37.23879	-115.013
404	Tkg	240	35	37.23789	-115.014
412	Tkv	15	30	37.25	-115.02
413	Th	250	25	37.25094	-115.021
427	Th	200	43	37.2342	-115.039

Measured faults:

Fault id.	Strike	Dip	Rake
155	181	73	
192	45	80	
195	140	80	
306	43	80	90SE
307	210	80	75NW
309	10	75	85E
319	85	85	90S
327	185	70	
405	187	81	
416	232	85	65E
420	185	75	86E
422	280	85	85N
424	10	45	55SSE

Calculated faults:

Fault id.	Strike	Dip
------------------	---------------	------------

1007	172	46
1008	177	61
1009	184	57
1010	162	50
1012	151	78
1013	180	90
1014	153	47
1030	164	27
1031	163	69
1038	178	33
1039	136	5

Table 3. Compaction foliation measurements collected along the Maynard Lake fault

Maynard Lake Fault Zone Data

Compaction Foliation Data:

Station #	Unit	Strike	Dip	Location	
12	Tkg	305	10	37.19981	-115.039
14	Tkg	290	24	37.20171	-115.035
26	Tkg	280	35	37.19783	-115.038
28	Tkg	205	27	37.19645	-115.036
31	Tkg	300	39	37.19385	-115.034
32	Tkg	235	35	37.19369	-115.033
54	Tkg	350	27	37.19576	-115.022
56	Tkg	305	19	37.19747	-115.023
57	Tkg	330	11	37.19678	-115.023
58	Tkg	306	35	37.19988	-115.021
59	Tkg	45	22	37.19988	-115.021
64	Tkg	50	38	37.19602	-115.039
65	Tkg	48	25	37.19522	-115.039
66	Tkg	280	15	37.19578	-115.038
67	Tkg	230	10	37.19659	-115.036
69	Tkg	110	15	37.194	-115.04
70	Tkg	115	15	37.19324	-115.043
71	Tkg	40	10	37.19357	-115.041
73	Tkg	130	10	37.19285	-115.04
74	Tkg	90	15	37.19245	-115.039
79	Th	351	36	37.18884	-115.038
80	Tkg	290	56	37.18697	-115.045

122	Th	215	47	37.21384	-115.019
124	Th	233	33	37.21555	-115.018
125	Qo	24	13	37.21486	-115.016
127	Th	224	34	37.21794	-115.015
128	Th	262	29	37.21947	-115.013
129	Th	302	40	37.2193	-115.012
130	Th	312	22	37.22003	-115.012
131	Th	295	32	37.22003	-115.012
132	Th	270	22	37.22079	-115.012
136	Tkg	300	58	37.18721	-115.04
137	Th	280	30	37.22034	-115.012
138	Tkv	290	41	37.22348	-115.011
140	Tkv	348	89	37.22187	-115.01
144	Th	210	28	37.21702	-115.017
146	Th	290	33	37.21955	-115.016
147	Th	275	30	37.21973	-115.015
148	Th	356	80	37.22002	-115.015
150	Th	275	45	37.22225	-115.015
156	Tkg	220	28	37.20984	-115.026
157	Tkv	280	25	37.21406	-115.027
159	Th	190	30	37.21455	-115.025
160	Th	80	20	37.21449	-115.025
161	Th	190	28	37.21483	-115.025
162	Th	182	25	37.21588	-115.025
176	Th	140	22	37.22808	-115.004
177	Th	76	25	37.2281	-115.005
178	Th	75	15	37.22838	-115.005
181	Th	75	25	37.22921	-115.004
182	Th	160	5	37.23	-115.004
183	Th	30	40	37.23053	-115.003
184	Th	20	25	37.23046	-115.003
185	Tkv	40	21	37.22889	-115.002
187	Th	0	35	37.22984	-115.001
188	Th	30	15	37.232	-115
198	Th	15	23	37.22695	-115.011
199	Tkg	105	10	37.20102	-115.021
200	Tkg	50	15	37.20033	-115.02
201	Tkg	220	15	37.20182	-115.021
202	Tkg	170	10	37.20326	-115.019
203	Tkg	270	10	37.20325	-115.015
216	Tkg	315	28	37.2035	-115
222	B1	185	20	37.20069	-115.021
232	Th	220	40	37.21872	-115.01

233	Th	290	35	37.22	-115.006
236	Th	252	35	37.22035	-115.005
238	Tkv	320	40	37.22062	-115.004
247	Qo	110	15	37.20832	-115.04
261	Th	55	22	37.22909	-115.009
434	Th	150	40	37.22986	-115.002

Measured faults:

Fault id.	Strike	Dip	Rake
63	275	27	
72	85	5	
76	40	70	
77	25	55	
114	274	51	
115	247	20	
116	229	43	
117	272	45	
118	280	54	
119	244	71	
120	40	75	32S
121	223	86	44N
134	344	72	
139	5	81	
140	343	75	
143	225	82	
145	359	89	
146	310	41	
175	130	75	
179	330	85	
207	43	65	
208	35	75	
210	40	80	90SE
215	240	83	
231	76	80	
243	194	56	45N
431	200	65	90W
433	175	55	65S
444	40	85	

Calculated faults:

Fault id.	Strike	Dip
1015	305	36
1016	263	21

1017	269	18
1024	70	82
1025	144	10
1027	55	38
1027	55	38
1028	211	48
1029	37	50
1032	165	60
1036	225	76
1037	228	32

Table 4. Compaction foliation measurements collected from domain C

Domain C Data

Compaction Foliation

Data:

Station #	Unit	Strike	Dip	Location	
35	Tkg	305	5	37.18604	-115.016
36	Tkg	5	19	37.18443	-115.015
39	Tkg	260	35	37.18924	-115.007
40	Tkg	138	28	37.18963	-115.006
41	Tkg	173	27	37.18987	-115.006
45	Tkg	165	26	37.18605	-115.004
47	Tkg	144	9	37.18427	-115.009
62	Tkg	100	20	37.1818	-115.002
83	B2	315	14	37.19186	-115.009
84	B2	145	14	37.19159	-115.009
88	Tkg	205	22	37.18783	-115.007
93	Tkg	115	11	37.1962	-115.015
95	Tkg	340	16	37.18135	-115.016
96	Tkg	5	25	37.18084	-115.016
97	Tkg	334	25	37.17553	-115.015
99	Tkg	235	10	37.17242	-115.013
100	Tkg	310	9	37.17241	-115.013
101	B2	10	7	37.17189	-115.013
102	Tkg	255	12	37.17149	-115.013
103	Tkg	240	12	37.17148	-115.013
104	Tkg	75	25	37.17653	-115.016
105	Tkg	98	25	37.17672	-115.016
106	Tkg	55	35	37.17636	-115.016
107	Tkg	62	28	37.17624	-115.016
108	Tkg	horizontal		37.17849	-115.017
109	Tkg	335	10	37.17849	-115.017
110	Tkg	20	20	37.17936	-115.017
111	Tkg	350	10	37.18089	-115.018
112	Tkg	350	6	37.18476	-115.021
347	Th	295	18	37.19097	-115.03
357	Tkv	285	25	37.18731	-115.021
358	Tkg	330	22	37.1873	-115.021
360	Tkg	10	22	37.18602	-115.021
362	Qo2	260	6	37.18938	-115.022

Measured faults:

Fault id.	Strike	Dip	Rake
355	285	90	20NW
90	340	44	60NW
51	330	50	
89	326	50	90N

Calculated faults:

Fault id.	Strike	Dip
1018	214	64
1041	5	89
1042	354	71
1019	310	40
1020	171	88
1022	340	43
1023	337	32
1021	31	10

Appendix 2

Table 1. NIGL - Description and Procedures

Nevada Isotope Geochronology Laboratory - Description and Procedures

Kathleen Zanetti and Terry Spell

Samples analyzed by the $^{40}\text{Ar}/^{39}\text{Ar}$ method at the University of Nevada Las Vegas were wrapped in Al foil and stacked in 6 mm inside diameter sealed fused silica tubes. Individual packets averaged 2 mm thick and neutron fluence monitors (FC-2, Fish Canyon Tuff sanidine) were placed every 5-10 mm along the tube. Synthetic K-glass and optical grade CaF_2 were included in the irradiation packages to monitor neutron induced argon interferences from K and Ca. Loaded tubes were packed in an Al container for irradiation. Samples irradiated at the U. S. Geological Survey TRIGA Reactor, Denver, CO were in-core for 7 hours in the 1 MW TRIGA type reactor. Correction factors for interfering neutron reactions on K and Ca were determined by repeated analysis of K-glass and CaF_2 fragments. Measured $(^{40}\text{Ar}/^{39}\text{Ar})_{\text{K}}$ values were $1.36 (\pm 12.80\%) \times 10^{-2}$. Ca correction factors were $(^{36}\text{Ar}/^{37}\text{Ar})_{\text{Ca}} = 3.01 (\pm 0.80\%) \times 10^{-4}$ and $(^{39}\text{Ar}/^{37}\text{Ar})_{\text{Ca}} = 8.31 (\pm 0.44) \times 10^{-4}$. J factors were determined by fusion of 5-6 individual crystals of neutron fluence monitors which gave reproducibility's of 0.09% to 0.10% at each standard position. Variation in neutron fluence along the 100 mm length of the irradiation tubes was <4%. Matlab curve fit was used to determine J and uncertainty in J at each standard position. No significant neutron fluence gradients were present within individual packets of crystals as indicated by the excellent reproducibility of the single crystal fluence monitor fusions.

Irradiated FC-2 sanidine standards together with CaF₂ and K-glass fragments were placed in a Cu sample tray in a high vacuum extraction line and were fused using a 20 W CO₂ laser. Sample viewing during laser fusion was by a video camera system and positioning was via a motorized sample stage. Reactive gases were removed by three GP-50 SAES getters prior to being admitted to a MAP 215-50 mass spectrometer by expansion. The relative volumes of the extraction line and mass spectrometer allow 80% of the gas to be admitted to the mass spectrometer for laser fusion analyses. Peak intensities were measured using a Balzers electron multiplier by peak hopping through 7 cycles; initial peak heights were determined by linear regression to the time of gas admission. Mass spectrometer discrimination and sensitivity was monitored by repeated analysis of atmospheric argon aliquots from an on-line pipette system. Measured ⁴⁰Ar/³⁶Ar ratios were $297.61 \pm 0.04\%$ during this work, thus a discrimination correction of 0.9929 (4 AMU) was applied to measured isotope ratios. The sensitivity of the mass spectrometer was $\sim 6 \times 10^{-17}$ mol mV⁻¹ with the multiplier operated at a gain of 36 over the Faraday. Line blanks averaged 1.30 mV for mass 40 and 0.01 mV for mass 36 for laser fusion analyses. Discrimination, sensitivity, and blanks were relatively constant over the period of data collection. Computer automated operation of the sample stage, laser, extraction line and mass spectrometer as well as final data reduction and age calculations were done using LabSPEC software written by B. Idleman (Lehigh University). An age of 28.02 Ma (Renne et al., 1998) was used for the Fish Canyon Tuff sanidine fluence monitor in calculating ages for samples.

For each sample inverse isochron diagrams are examined to check for the effects of excess argon. Reliable isochrons are based on the MSWD criteria of Wendt and Carl (1991). All analytical data are reported at the confidence level of 1 σ (standard deviation).

Appendix 3

Table 1. ¹⁴C dates from Qaf

Sample	Conventional Age BP	Calendar Calibration at 95.4% probability level	Percent Modern Carbon (pMC)	Location Taken	
				Lat	Long
449	8560 +/- 30	7601 - 7546 cal BC 9550 - 9495 cal BP	34.45 +/- 0.13	37.194298	-115.053948
450	9050 +/- 30	8296 - 8241 cal BC 10245 - 10190 cal BP	32.41 +/- 0.12	37.194722	-115.057423
Samples taken 12/12/2017					
Calendar Calibration at 95.4% probability level					

Table 2. $^{40}\text{Ar}/^{39}\text{Ar}$ dating of Kane Wash Tuff Gregerson Member sample 385/386

Peck-UNLV, Sample 385/386, Single Crystal Fusion, Sanidine, J = 0.001757 ± 0.40%												
4 amu discrimination = 0.9929 ± 0.04%, 40/39K = 0.0136 ± 12.80%, 36/37Ca = 0.000301 ± 0.80%, 39/37Ca = 0.000831 ± 0.44%												
Crystal	T (C)	t (min.)	36Ar	37Ar	38Ar	39Ar	40Ar	%40Ar *	Ca/K	40Ar*/39ArK	Age (Ma)	1s.d.
1	160 0	1	0.02 5	0.30 1	0.47 6	36.641	183.607	97.3	0.0453846	4.8299	15.25	0.08
2	160 0	1	0.06 7	0.35 1	0.68 7	50.560	262.807	93.3	0.0383538	4.8133	15.19	0.09
3	160 0	1	0.03 6	0.45 5	0.89 6	69.187	340.953	97.5	0.0363325	4.7742	15.07	0.07
4	160 0	1	0.07 9	0.24 2	0.34 3	25.841	148.754	85.8	0.0517388	4.8872	15.43	0.07
5	160 0	1	0.03 9	0.18 3	0.32 6	24.180	126.667	92.9	0.0418123	4.8032	15.16	0.07
6	160 0	1	0.01 8	0.20 3	0.35 0	26.282	131.492	97.9	0.0426724	4.8388	15.27	0.07
7	160 0	1	0.05 2	0.30 7	0.53 1	39.883	206.236	93.7	0.0425265	4.8016	15.16	0.08
8	160 0	1	0.07 1	0.35 6	0.61 8	45.861	235.691	92.0	0.042886	4.6918	14.81	0.07
9	160 0	1	0.05 7	0.17 5	0.31 1	22.739	129.164	88.8	0.0425183	4.9829	15.73	0.07
10	160 0	1	0.11 6	0.19 7	0.26 6	18.987	127.544	74.8	0.057322	4.9626	15.66	0.08
11	160 0	1	0.05 8	0.19 7	0.31 9	21.905	121.632	87.9	0.0496859	4.8165	15.20	0.07
12	160 0	1	0.03 7	0.19 2	0.33 9	25.080	131.306	93.6	0.0422944	4.8388	15.27	0.08
13	160	1	0.04	0.20	0.33	25.039	134.334	91.5	0.0443495	4.8512	15.31	0.09

	0		4	1	7							
14	160 0	1	0.06 9	0.24 3	0.29 7	24.010	134.881	86.0	0.0559146	4.7733	15.07	0.08
15	160 0	1	0.10 8	0.41 0	0.62 9	48.236	270.273	88.6	0.0469594	4.9308	15.56	0.07
16	160 0	1	0.06 5	0.22 2	0.36 7	26.837	147.142	87.9	0.0457013	4.7691	15.05	0.14
17	160 0	1	0.04 1	0.25 8	0.45 5	32.988	174.257	93.9	0.0432089	4.9139	15.51	0.07
18	160 0	1	0.07 1	0.29 0	0.43 5	31.165	172.206	88.6	0.0514093	4.8509	15.31	0.08
19	160 0	1	0.02 6	0.14 7	0.22 8	16.538	85.719	93.1	0.0491071	4.7408	14.97	0.12
20	160 0	1	0.02 4	0.43 6	0.56 1	40.855	204.222	97.3	0.0589594	4.8213	15.22	0.07
21	160 0	1	0.15 6	0.47 4	0.47 7	34.212	189.448	82.6	0.0765445	4.5341	14.32	0.31
22	160 0	1	0.20 4	0.20 5	0.37 2	24.805	183.044	67.6	0.0456588	4.9409	15.59	0.08
23	160 0	1	0.01 2	0.11 8	0.22 3	17.048	84.481	97.9	0.03824	4.7694	15.06	0.14
24	160 0	1	0.12 9	0.24 2	0.43 9	30.020	158.973	76.2	0.0445363	3.9909	12.61	0.21
25	160 0	1	0.15 1	0.39 6	0.62 0	43.291	253.828	82.4	0.0505368	4.7806	15.09	0.07
26	160 0	1	0.02 1	0.18 4	0.34 4	25.360	127.821	95.7	0.0400846	4.7653	15.04	0.09
note: isotope beams in mV rlsd = released, error in age includes J error, all errors 1 sigma										Mean ± s.d. =	15.11	0.59
(36Ar through 40Ar are measured beam intensities, corrected for decay in age calculations)										Mean ± s.d. =	15.21	0.09
										(xtal 24 omitted)		
										Wtd mean age =	15.17	0.03
										(18 fusions)		

	No isochron
--	-------------

Table 3. $^{40}\text{Ar}/^{39}\text{Ar}$ dating of Kane Wash Tuff Gregerson Member sample 388

Peck-UNLV, Sample 388, Multiple Crystal Fusion, Sanidine, J = 0.001788 ± 0.38%												
4 amu discrimination = 0.9879 ± 0.08%, 40/39K = 0.0136 ± 12.80%, 36/37Ca = 0.000301 ± 0.80%, 39/37Ca = 0.000831 ± 0.44%												
Fusion	T (C)	t (min.)	36Ar	37Ar	38Ar	39Ar	40Ar	%40Ar*	Ca/K	40Ar*/39ArK	Age (Ma)	1s.d.
1	160 0	1	0.03 4	0.18 1	0.32 8	23.884	126.061	93.3	0.0362813	4.8446	15.56	0.09
2	160 0	1	0.02 3	0.14 7	0.23 8	15.989	86.067	94.1	0.0440158	4.9553	15.91	0.12
3	160 0	1	0.01 9	0.22 7	0.26 3	19.840	106.703	96.4	0.054777	5.0883	16.34	0.08
4	160 0	1	0.03 2	0.18 6	0.32 6	25.548	136.784	94.2	0.0348552	4.9700	15.96	0.07
5	160 0	1	0.10 0	0.12 3	0.29 9	21.589	137.134	79.3	0.0272761	4.9607	15.93	0.08
6	160 0	1	0.02 7	0.10 0	0.16 1	12.356	75.321	91.7	0.0387466	5.4532	17.51	0.17
note: isotope beams in mV rlsd = released, error in age includes J error, all errors 1 sigma. (36Ar through 40Ar are measured beam intensities, corrected for decay in age calculations)										Mean ± s.d. =	16.20	0.68
										Wtd mean age =	15.94	0.05
										(3 fusions), no isochron		

Appendix 4

Table 1. Earthquake magnitude calculations

Wells and Coppersmith		
$M = 4.38 + 1.49 \cdot \log(SRL)$		Moment magnitude
	Length km	
Total length	36.4	6.9
SW segment	9.6	6.2
Central segment	21	6.6
NE segment	5.8	6.0

Hanks and Bakun				
$M = \log A + 3.98$				Moment magnitude
	Length km	Depth km	area sqkm	
Total length	36.4	10	364	6.5
SW segment	9.6	10	96	6.0
Central segment	21.0	10	210	6.3
NE segment	5.8	10	58	5.7

Anderson et al.			
$M = 5.12 + 1.16 \log L - 0.20 \log S$			Moment magnitude
	Length km	Slip mm/yr	
Total length	36.4	1.8	6.9
SW segment	9.6	1.8	6.2
Central segment	21	1.8	6.6
NE segment	5.8	1.8	6.0

References

- Anderson, G.J., Wesnousky, S.G., and Stirling, M.W., 1996, Earthquake size as a function of fault slip rate: *Bulletin of the Seismological Society of America*, v. 86, p. 683-690.
- Axen, G.J., 1998, The Caliente-Enterprise zone, southeastern Nevada and southwestern Utah: *Geological society of America special paper*, v. 323, p. 181–194.
- Axen, G.J., Taylor, W.J., and Bartley, J.M., 1993, Space-time patterns and tectonic controls of Tertiary extension and magmatism in the Great Basin of the western United States: *Geological Society of America Bulletin*, v. 105, p. 56–76.
- Best, M.G., Barr, D.L., Christiansen, E.H., Gromme, S., Deino, A.L., and Tingey, D.G., 2009, The Great Basin Altiplano during the middle Cenozoic ignimbrite flareup: insights from volcanic rocks: *International Geology Review*, v. 51, p. 589–633, doi: 10.1080/00206810902867690.
- Best, M.G., Christiansen, E.H., and Gromme, S., 2013, Introduction: The 36–18 Ma southern Great Basin, USA, ignimbrite province and flareup: Swarms of subduction-related supervolcanoes: *Geosphere*, v. 9, p. 260–274.
- Best, M.G., Scott, B., Rowley, P.D., Swadley, W.C., Anderson, R.E., Gromme, S.C., Harding, A.E., Deino, A.L., Christiansen, E.H., Tingey, D.G., and Sullivan, K.R., 1993, Crustal evolution of the Great Basin and the Sierra Nevada: *Field Trip Guidebook for the 1993 Joint Meeting of the Cordilleran/Rocky Mountain Sections of the Geological Society of America*, Reno, Nevada, p. 285-381.
- Beta Analytic Radiocarbon Dating <https://www.radiocarbon.com/>
- Bidgoli, T.S., Stockli, D.F., and Walker, J.D., 2015, Low-temperature thermochronologic constraints on the kinematic histories of the Castle Cliffs, Tule Springs, and Mormon Peak detachments, southwestern Utah and southeastern Nevada: *Geosphere*, v. 11, p. 850–867.
- Colgan, J. P., Dumitru, T. A., Reiners, P. W., Wooden, J. I., and Miller, E.I., 2006, Cenozoic Tectonic evolution of the Basin and Range Province in Northwestern Nevada: *American Journal of Science*, v. 306, p. 616-654.
- DePolo, D.M., and dePolo, C.M., 2012, Earthquakes in Nevada: 1840s to 2010: Nevada Bureau of Mines and Geology M 179, 1 plate.
- Ekren, E.B., Bucknam, R.C., Carr, W.J., Dixon, G.L., and Quinlivan W.D., 1976, East-trending structural lineaments in central Nevada: *Geological Survey Professional Paper 986*, 16 pp., 1 plate.

- Ely, R., **Peck, A.**, Christensen, A., Kassela, M., Martin, K., Price, T., Abdelhaleem, S., and Taylor, W.J., Preliminary geologic map of Alamo SE Quadrangle, Lincoln County, Nevada: Nevada Bureau of Mines and Geology.
- Evans, M.D., 2017, Structural evolution and regional implications of the Arrowhead Mine fault within the Pahranaगत shear zone, Nevada, USA: UNLV M.S. thesis, 79 pp.
- Faulds, J.E., and Varga, R.J., 1998, The role of accommodation zones and transfer zones in the regional segmentation of extended terranes: Geological society of America Special Paper 323, p. 1–45.
- Grasemann, B., Martel, S., and Passchier, C., 2005, Reverse and normal drag along a fault: *Journal of Structural Geology*, v. 27, p. 999–1010, doi: 10.1016/j.jsg.2005.04.006.
- Hanks, T.C., and Bakun, W.H., 2002, A bilinear source-scaling model for M-log A observations of continental earthquakes: *Bulletin of the Seismological Society of America*, v. 92, p. 1841–1846.
- Hanks, T.C., and Bakun, W.H., 2008, M-logA observations for recent large earthquakes: *Bulletin of the Seismological Society of America*, v. 98, p. 490–494, doi: 10.1785/0120070174.
- Hudson, H.R., Rosenbaum, J., Gromme, C.S., Scott, R.B., and Rowley, P.D., 1998, Paleomagnetic evidence for counterclockwise rotation in a broad sinistral shear zone, Basin and Range Province, southeastern Nevada and southwestern Utah : *Geological society of America special paper*, v. 323, p. 213–236.
- Jayko, A.S., 1990, Shallow crustal deformation in the Pahranaगत area, southern Nevada: *Geological Society of America Memoirs*, v. 176, p. 213–236.
- Kase, Y., and Kuge, K., 2001, Rupture propagation beyond fault discontinuities: significance of fault strike and location: *Geophysical Journal International*, v. 147, p. 330–342.
- Kreemer, C., Blewitt, G., and Hammond, W.C., 2010, Evidence for an active shear zone in southern Nevada linking the Wasatch fault to the Eastern California shear zone: *Geology*, v. 38, p. 475–478.
- Lettis, W., Bachhuber, J., Witter, R., Brankman, C., Randolph, C.E., Barka, A., Page, W.D., and Kaya, A., 2002, Influence of releasing step-overs on surface fault rupture and fault segmentation: Examples from the 17 August 1999 Izmit earthquake on the North Anatolian fault, Turkey: *Bulletin of the Seismological Society of America*, v. 92, p. 19–42.
- Muhammad, M.M., 2016, Structural Evolution of the Maynard Lake Fault within the Left-Lateral Pahranaगत shear zone, Nevada, USA: UNLV M.S. thesis, 79 pp.

- Oglesby, D., 2008, Rupture termination and jump on parallel offset faults: *Bulletin of the Seismological Society of America*, v. 98, p. 440–447, doi: 10.1785/0120070163.
- Oglesby, D.D., 2005, The dynamics of strike-slip step-overs with linking dip-slip faults: *Bulletin of the Seismological Society of America*, v. 95, p. 1604–1622, doi: 10.1785/0120050058.
- Peacock, D.C.P., 2002, Propagation, interaction and linkage in normal fault systems: *Earth-Science Reviews*, v. 58, p. 121–142.
- Petronis, M.S., Holm, D.K., Geissman, J.W., Hacker, D.B., and Arnold, B.J., 2014, Paleomagnetic results from the eastern Caliente-Enterprise zone, southwestern Utah: Implications for initiation of a major Miocene transfer zone: *Geosphere*, v. 10, p. 534–563.
- Price, T.G., 2017, Miocene-Pliocene(?) folds and normal faults associated with the left-lateral Buckhorn fault and regional implications, Pahrnagat shear zone, Nevada: UNLV M.S. thesis, 56 pp.
- Rowley, P.D., Nealey, L.D., Unruh, D.M., Snee, L.W., Mehnert, H.H., Anderson, R.E., and Gromme, C.S. (1992), Stratigraphy of Miocene Ash-Flow Tuffs in and near the Caliente Caldera Complex, Southern Nevada and Southwestern Utah: *U.S. Geological Survey Bulletin*, 2056, p. 47-88.
- Ryan, W.B.F., S.M. Carbotte, J.O. Coplan, S. O'Hara, A. Melkonian, R. Arko, R.A. Weissel, V. Ferrini, A. Goodwillie, F. Nitsche, J. Bonczkowski, and R. Zemsky (2009), Global Multi-Resolution Topography synthesis: *Geochemical. Geophysics. Geosystems.*, v. 10, Q03014, doi:10.1029/2008GC002332.
- Scott, R.B., Page, W.R., and Swadley, W C., 1990, Preliminary geologic map of the Delamar 3 NW quadrangle, Lincoln County, Nevada: *U.S. Geological Survey Geologic Quadrangle Map OF-90-405*, scale 1:24,000.
- Scott, S.W., and Swadley, W.C., 1992, *Geologic Studies in the Basin and Range-Colorado Plateau Transition in Southeastern Nevada, Southwestern Utah, and Northwestern Arizona*: *U.S. Geological Survey Bulletin* 2056, p. 1-4.
- Scott, S.W., Swadley, W.C., and Novak, S.W., 1993, *Geologic map of the Delamar Lake Quadrangle, Nevada*: *U.S. Geological Survey Geologic Quadrangle Map GQ-1730*, 1:24,000 scale.
- Sonder, L.J., and Jones, C.H., 1999, Western United States extension: How the west was widened: *Annual Review of Earth and Planetary Sciences*, v. 27, p. 417–462.

- Taylor, W.J. and Bartley, J.M., 1992. Prevolcanic extensional Seaman breakaway fault and its geologic implications for eastern Nevada and western Utah: Geological Society of America Bulletin, v. 104, p. 255-266.
- Taylor, W.J., Bartley, J.M., Martin, M.W., Geissman, J.W., Walker, J.D., Armstrong, P.A., and Fryxell, J.E., 2000, Relations between hinterland and foreland shortening: Sevier orogeny, central North American Cordillera: Tectonics, v. 19, p. 1124-1143.
- Tschanz, C.M., and Pampeyan, E.H., 1970, Geology and mineral deposits of Lincoln County, Nevada: Nevada Bureau of Mines and Geology Bulletin 73, 188 pp.
- U.S. Geological Survey and Nevada Bureau of Mines and Geology, 2006, Quaternary fault and fold database for the United States, accessed 02-10-2018, from USGS web site: <http://earthquake.usgs.gov/hazards/qfaults/>.
- Wells, D.L., and Coppersmith, K.J., 1994, New empirical relationships among magnitude, rupture length, rupture width, rupture area, and surface displacement: Bulletin of the Seismological Society of America, v. 84, p. 974–1002.
- Wernicke, B., 1992, Cenozoic extensional tectonics of the U.S. Cordillera: Geological Society of America, The Geology of North America, The Cordilleran Orogen: Conterminous U.S., The Decade of North American Geology (DNAG), v. G-3, p. 553-581.
- Zandt, G., and Humphreys, E., 2008, Toroidal mantle flow through the western US slab window: Geology, v. 36, p. 295–298.

Curriculum Vitae

Alexander M. Peck

antinovap@yahoo.com

EDUCATION

University of Nevada Las Vegas

M.S. in Geoscience: Expected completion April 2018

Research: Miocene-Quaternary deformation, eastern Pahranaगत shear zone, southern Nevada

Graduate research advisor: Dr. Wanda J. Taylor (wanda.taylor@unlv.edu)

Geoscience Teaching Assistant: GEOL 101 (Principles of Geology) 2017, GEOL 348 (Field Geology) 2016, GEOG 104 (Geography) 2015 – 2016, 2017, on-line & in-class

Bachelor of Science in Geology

Undergraduate research: Deformation of Miocene tuffs and sedimentary rocks, western Pahranaगत shear zone, southern Nevada; advisor: Dr. Wanda J. Taylor

PUBLICATIONS

Price, T., Evans, M., Muhammad, M., Hinson, M., McIntyre, R.A., **Peck, A.**, and Taylor, W.J., 2018, Preliminary geologic map of the Lower Pahranaगत Lake NW 7.5' Quadrangle, Lincoln County, Nevada: Nevada Bureau of Mines and Geology, 1:24,000 scale.

PUBLICATIONS PENDING

2018 submission, Ely, R., **Peck, A.**, Christensen, A., Kassela, M., Martin, K., Price, T., Abdelhaleem, S., and Taylor, W.J., Preliminary geologic map of Alamo SE Quadrangle, Lincoln County, Nevada: Nevada Bureau of Mines and Geology.

ABSTRACTS WITH PRESENTATIONS

Peck, A. and Taylor, W. J., 2017 New Evidence supporting probable earthquake nucleation site along the central Maynard Lake fault within the left-lateral Pahranaagat shear zone, Nevada, USA: Geological Society of America Abstracts with Programs. v. 49, no. 6, doi: 10.1130/abs/2017AM-307133; Oral Presentation.

Taylor, W. J., Chameroy, E.J., Ely, R.N., Konkright, K.J., Medema, J., **Peck, A. M.**, and Rafferty, K.C., 2017, Seismic Hazard and Paleoseismicity in southern Nevada: The California Wash Fault: Geological Society of America Abstracts with Programs. v. 49, no. 6, doi:10.1130/abs/2017AM-300654, Poster Presentation